Article:
Alodia, G, Green, CM orcid.org/0000-0001-9644-4949 and McCaig, AM orcid.org/0000-0001-7416-4911 (2022) SWE_of_Bathymetry.m: A geomorphometric tool to automate discrimination between detachment and magmatic seafloor at slow-spreading ridges from shipboard multibeam bathymetry. Computers and Geosciences, 166. 105177. ISSN 0098-3004

https://doi.org/10.1016/j.cageo.2022.105177

SWE_of_Bathymetry.m: A geomorphometric tool to automate discrimination between detachment and magmatic seafloor at slow-spreading ridges from shipboard multibeam bathymetry

Gabriella Alodia[a], Chris M. Green[b] and Andrew M. McCaig[c]

[a]Hydrography Research Group, Faculty of Earth Sciences and Technology, Institut Teknologi Bandung, Indonesia / School of Earth and Environment, University of Leeds, UK, ORCID(s): 0000-0002-7177-4033

[b]School of Earth and Environment, University of Leeds, UK / GETECH plc., Leeds, UK, ORCID(s): 0000-0001-9644-4949

[c]School of Earth and Environment, University of Leeds, UK, ORCID(s): 0000-0001-7416-4911

ARTICLE INFO

Keywords:

Geomorphometry

Multibeam bathymetry

Abyssal hills

Oceanic core complex

Slow-spreading ridge

Authorship contribution statement

Gabriella Alodia (GA): GA initiated the study, established the algorithm, and wrote the manuscript. Chris M. Green (CMG): CMG supervised the establishment of the algorithm and reviewed the manuscript. Andrew M. McCaig (AMM): AMM supervised the establishment of the algorithm and reviewed the manuscript.

ABSTRACT

The shapes and directionality of the oceanic crust at slow-spreading ridges are key to understanding its magmatic or tectonic emplacement. At slow-spreading ridges, magmatic terrain is marked by linearly fault-bounded abyssal hills, while a more tectonic emplacement termed detachment terrain is marked by long-lived detachment faults forming Oceanic Core Complexes (OCCs). However, the quantitative description of the magmatic and detachment regimes is still limited. We develop a novel geomorphometric technique to automate terrain classification based on the parameterisation of the shape, directionality, and curvature of the seafloor. The algorithm consists of two steps: (1) characterising the pattern observed in the horizontal axes by computing the horizontal eigenvalues of the slope vectors at each multibeam cells and (2) building a weight matrix derived from the computed slopes. The eccentricity of the horizontal eigenvalues defines the dipping pattern in the horizontal axes, hence the term slope-weighted eccentricity (SWE). The technique is applied through a moving window and is tested at 12.5°-15.5° N on the Mid-Atlantic Ridge (MAR), where the two distinct modes of spreading occur. The application of this novel geomorphometric technique yields results consistent with published qualitative interpretation and the distribution of seismicity observed from the peak amplitudes of the tertiary waves (T-waves) in the study area. Using the established algorithm, we found that 41% of the seafloor in our study area experienced detachment faulting (up to 28% are identified as OCCs), 25% experienced typical magmatic accretion, and a buffer zone termed extended terrain affects 34% of the seafloor, where the morphology shows a transition from detachment to magmatic spreading or vice versa. These findings provide new insights into seafloor classification based on the observed morphology and the potential to automate such mapping at other slow-spreading ridge regions.

1. Introduction

Parts of slow-spreading ridges have been described as experiencing typical magmatic accretion where fault-bounded abyssal hills form symmetrically at both flanks of the spreading axis (Macdonald, 1982). Elsewhere, asymmetric accretion is observed where volcanic flows form on one flank and detachment faults form on the opposing flank (Rona et al., 1987; Smith, 2013). These atypical, curved faults form a dome-shaped seafloor, termed oceanic core complexes (OCCs), in which lower-crustal and mantle rocks are exhumed (Blackman et al., 2009; Cann et al., 1997; Dannowski et al., 2010; MacLeod et al., 2002). The OCC morphology contrasts with the linearly fault-bounded abyssal hills resulting from a magmatic accretion (Mutter and Karson, 1992; Sinton and Detrick, 1992), indicating the complex interaction between the magmatic and tectonic regimes (Escartín and Cannat, 1999). The type of spreading has been termed 'detachment mode' (McCaig and Harris, 2012) or, more generally, 'tectonic' spreading (e.g., Cann et al., 2015). It has been suggested that up to 50% of Atlantic seafloor may have formed in the detachment mode (Escartín et al., 2008), but this has not been fully quantified.

Identification of different types of spreading terrain has been attempted based on qualitative observation of shipboard multibeam bathymetry, often paired with rock sampling through dredging, drilling, and sample collecting using submersible vehicles (e.g., Cannat et al., 1992; Lagabrielle et al., 1998; Schroeder et al., 2007) as well as other geophysical surveys such as gravity, magnetic, and seismic surveys (e.g., Dannowski et al., 2010; Pockalny et al., 1995; Tivey and Dyment, 2013). This study aims to aid the identification by establishing a tool to automate the detachment and magmatic crust classification through a series of quantitative terrain characterisation, or the geomorphometry, of detachment and magmatic seafloor. We introduce an algorithm termed 'slope-weighted eccentricity' (SWE) as a novel geomorphometric technique that can be applied in slow-spreading ridges to characterise the distribution of the detachment and magmatic regimes in specific regions.

The first comprehensive overview of marine geomorphometry efforts carried out to date is presented in Lecours et al. (2016). Seabed feature identification such as pockmarks (Gafeira et al., 2012; Harrison et al., 2011), submarine canyons (Green and Uken, 2008; Ismail et al., 2015; Micallef et al., 2012), and terraces (Passaro et al., 2011) have been made available from the derivation and statistical characterisation of multibeam bathymetry data. At mid-ocean ridges, seabed characterisation has been attempted, for example, by Smith and Shaw (1989), Goff et al. (1995), and Chakraborty et al. (2001). Specifically, a quantitative characterisation of abyssal hill terrain has been attempted by

Goff et al. (1995) by describing multibeam data with three physical parameters, namely the rms (root-mean-square) height, characteristic width, and plan view aspect ratio (Goff and Jordan, 1988). The study manages to characterise the relation between the spreading mechanism and resulting morphology, where abyssal hills originating at inside corners of ridge-transform intersections have larger rms height, larger characteristic width, and smaller plan view aspect ratio compared to those originating at outside corners of ridge-transform intersections. In addition, the study also found the relation between the resulting abyssal hills morphology with the thickness of the crust derived from residual mantle Bouguer anomaly (RMBA), where lower-relief, narrower, and more lineated abyssal hills are formed when the crust is thicker while higher, wider, less lineated abyssal hills are formed when the crust is thinner.
In line with the plan view aspect ratio method, we develop an algorithm that exploits the directionality and steepness of the terrain, both derived from multibeam data. We argue that the quantification of massif-shaped OCCs and linearly bounded abyssal hills through their directional eigenvalue explored in this study serves as a novel and supporting method to the previously developed techniques.

The algorithm is built based on three of the four main types of terrain attributes described in Wilson et al. (2007), which are the slope, orientation, and curvature of the seafloor. We exploit the plunge (slope) and azimuth (orientation) of the slope vectors computed from bathymetry over features of interest and their distribution in a spherical coordinate system (Watson, 1965; Woodcock, 1977), as well as a simplified form of azimuth rose, termed eigenvalue ellipse. The algorithm is applied to a gridded shipboard multibeam bathymetry data set using a moving window, which window size is determined through a series of sensitivity tests.

From our observation, we follow Cann et al. (2015) in adding in the ‘extended terrain,’ which represents an area where both bidirectional and omnidirectional dipping slopes exist, showing the transition between the two crustal regimes. Furthermore, we exploit the curvatures of the seafloor to identify individual OCCs using a mask created from a Laplacian-of-Gaussian-filtered (LoG-filtered) bathymetry. A radially symmetric Gaussian filter, with a diameter reflecting the general size of the feature of interest, is applied to generalise the morphology of the seafloor. Subsequently, the Laplacian filters determines whether the feature is concave down (e.g., a dome) or concave up (e.g., a local basin). The automatically classified seafloor and the identified individual OCCs will then act as a novel means to provide insights into the processes that occur in a slow-spreading ridge through time.

2. Study area

We select an area with available shipboard multibeam bathymetry data over ~5 Ma between the Marathon and Fifteen-Twenty fracture zones (12.5°-15.5° N). The extent of the area can be seen in Figure 1. The gridded bathymetry is provided by D. K. Smith through personal contact and is a combination of multiple shipboard multibeam surveys carried out by Escartín and Cannat (1999) along the Fifteen-Twenty fracture zone (~15° 20' N) and its two adjacent ridge axes, by Fujiwara et al. (2003) from ~14° N up to the Fifteen-Twenty fracture zone, and by Smith et al. (2006) from ~14° N down to the Marathon fracture zone (~12° 40' N). The original combined bathymetry was gridded by D. K. Smith with a cell size of 200 m.

Seismicity in the area has been recorded by an array of autonomous hydrophones moored on the flanks of the Mid-Atlantic Ridge (MAR) between 15° N and 35° N (Escartín et al., 2003; Smith et al., 2003; Smith et al., 2002). Earthquakes' locations are derived from the peak amplitudes of the tertiary waves (T-waves) observed in the vicinity of the hydrophones. The derived locations may coincide with earthquake epicentres, but factors such as morphology, the velocity structure of the crust, and the depth of the earthquake below the seafloor may bias the calculation. Hence, the derived locations are not termed 'epicentres' but rather 'T-wave source locations' (Fox et al., 2001).

The distribution of the observed seismicity reflects the tectonism in the area, where continuous seismicity is found close to the bounding fracture zones while a seismic gap is found in the middle of the area, or around 14° N (Escartín et al., 2003). The seismic gap at the segment is consistent with a continuous zone of high acoustic backscatter and a magmatically-robust morphology, marked by the presence of long abyssal hills parallel to the spreading axis. In contrast, the continuous seismicity at the segment ends (13° N and 15° N) occurs in terrain with much rougher topography where sporadic massifs are in place (Smith et al., 2008). The broadly scattered seismicity along the axis is thought to be associated with slip on detachment faults (Smith et al., 2006). Furthermore, the observation is consistent with the indication of brittle rupture at depths up to 10-12 km below the seafloor near the ends of spreading segments by means of teleseismic and microearthquake studies (Bergman and Solomon, 1990; Kong et al., 1992; Wolfe et al., 1995).

The abundant samples of ultramafic rocks close to the massifs at both 13° N and 15° N segments (Cannat et al., 1997; MacLeod et al., 2009; Rona et al., 1987) demonstrate the domination of the OCC formation specifically in these two segments. The study of Smith et al. (2008) explores fault rotation and core complex formation in the region, where steep outward-facing slopes of the footwalls of many of the normal faults have rotated more than 30 degrees, indicating a large amount of tectonic extension. The steep fault resulting from the rotation typically grades into smoother dome-shaped seafloor, in which an OCC may develop. The dome-shaped seafloor is commonly elevated compared to the surrounding seafloor. In contrast, the abyssal hills formed at the 14° N segment display a smaller amount of rotation, typically less than 15 degrees.

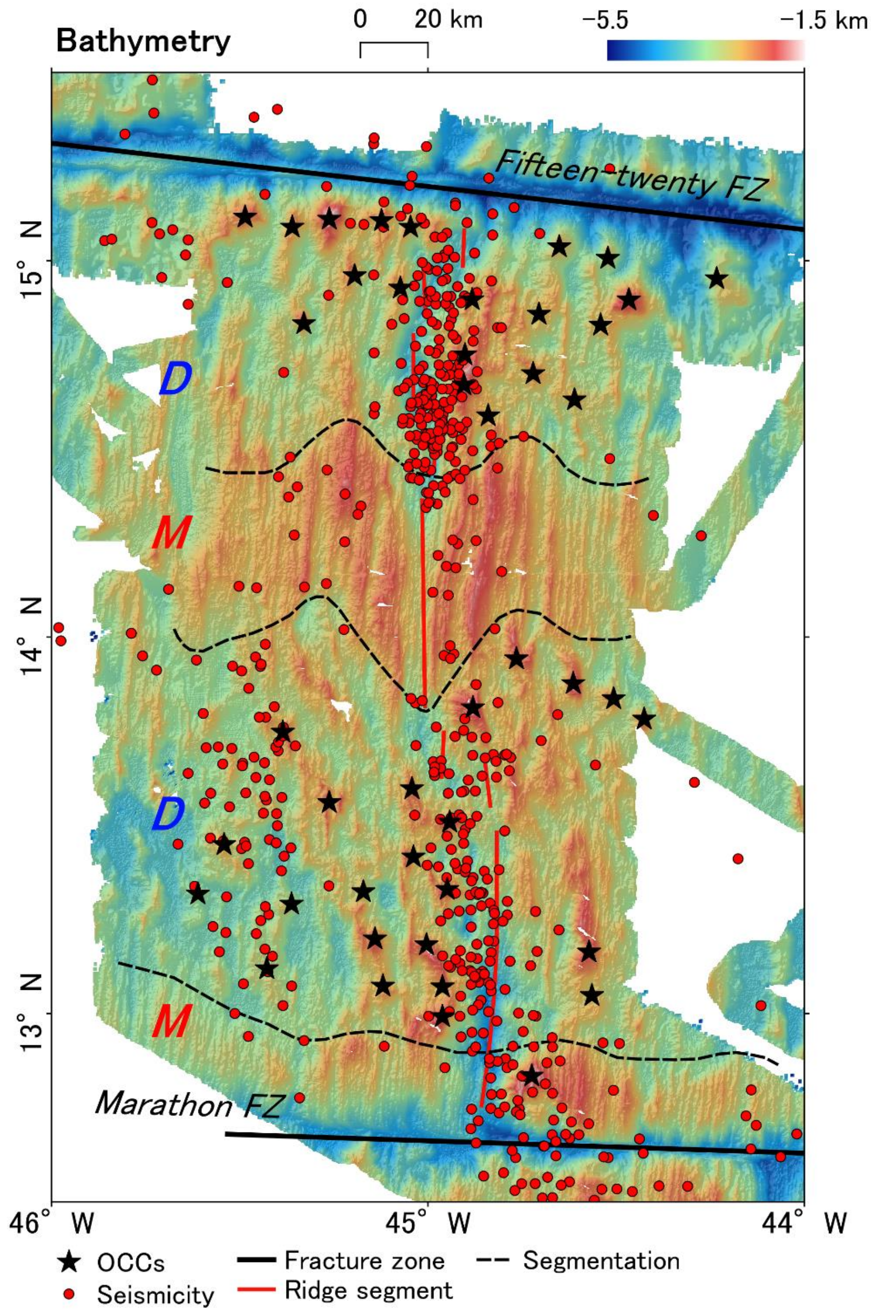

Figure 1 Bathymetric map of the study area. The combined data originates from cruises documented in Escartín and Cannat (1999), Fujiwara et al. (2003), and Smith et al. (2006). Segmentation (black dashed lines) is inferred by Smith et al. (2008), dividing the area into detachment (D) and magmatic (M) terrain. Black stars: inferred OCCs (Smith et al., 2008). Red dots: T-wave origin seismicity (Smith et al., 2003). Black lines: fracture zones. Red lines: ridge segments.

3. Slope-weighted eccentricity

The slope-weighted eccentricity (SWE) is a geomorphometric algorithm created to obtain the numerical description of both detachment and magmatic crust through a series of calculations based on the distribution of the azimuth and plunge of the slope vector, which is the steepest line within the seafloor surface at any point. The calculation is applied to a set of gridded multibeam bathymetry data through a moving window, starting from the top-left corner down to the bottom-right corner of the grid. In this section, we explain the fundamental theories on which the calculation is based, starting from the description of a spherical coordinate system, eigenvalues of the slope vectors and their graphical representation, eigenvalue ellipse and eccentricity as a means of describing the horizontal pattern of a terrain window, and the introduction of slope as a weight matrix. In addition, we use the Laplacian-of-Gaussian (LoG) filters (e.g., Huertas and Medioni, 1986) to define the generalised curvatures of the seafloor. The defined curvatures will serve as a means to highlight the concave down morphology of both magmatic abyssal hills and OCCs and mask out the concave up morphology to identify individual OCCs.

3.1. Spherical coordinate system

The gridded multibeam bathymetry comprises data cells of longitude, latitude, and height (lon, lat, h). From the gridded data set, we compute the azimuth (α) and plunge (θ) of the mean slope vector within each cell using the built-in *aspect* and *slope* functions in Matlab, respectively. In the functions, azimuth is calculated by considering the horizontal deviation of dip relative to the north (0°), while the plunge is calculated by analysing the depth gradient of each cell of a gridded surface relative to a plane surface. In this function, the plunge is described as positive down ($+\theta$ down) from the horizon to the nadir (+0° to +90°). Therefore, to match the spherical coordinate system, the sign is reversed ($-\theta$), so the values are all ≤ 0° (see Figure 2). From the azimuth and plunge grids, the slope vectors are described in its Cartesian representations of the tangent surface to the grid at each point (Tx, Ty, Tz) by:

$$Tx = \sin\alpha\cos(-\theta)$$

$$Ty = \cos\alpha\cos(-\theta\,) \qquad (1)$$

$$Tz = \sin(-\theta)$$

A window of multiple cells (Tx_i, Ty_i, Tz_i) is then defined (see Figure 2) to observe the directional trend on a sampled terrain. By plotting (Tx_i, Ty_i, Tz_i) coordinates in a spherical coordinate system, we can see approximately where these points are distributed and about which axis they are most clustered (see Watson, 1965; Woodcock, 1977). This distribution can be numerically described by computing the three-dimensional eigenvalues in each windowed terrain.

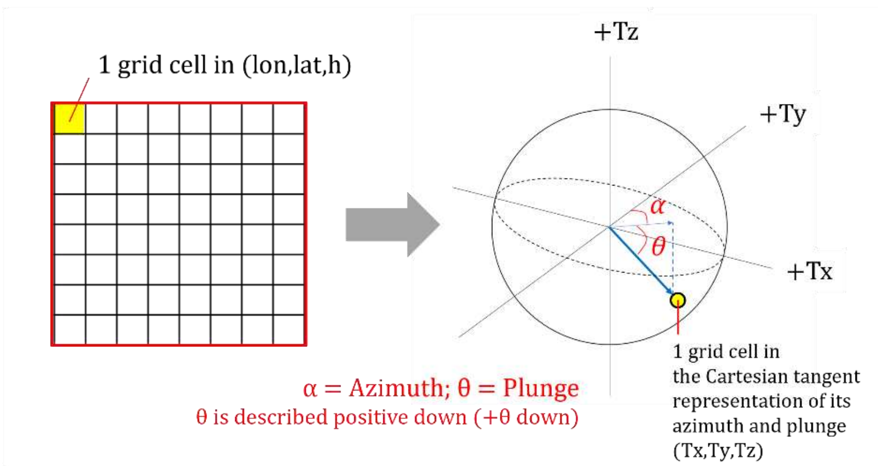

Figure 2 Illustration of how a window of terrain with cells described as (lon, lat, h) is converted into a spherical coordinate system containing azimuth and plunge values. Firstly, the terrain window is computed into two separate windows of azimuth (α) and plunge (θ) using the built-in *aspect* and *slope* functions in Matlab, respectively. Afterwards, the azimuth and plunge of the slope vectors are used to compute the Cartesian representations of the tangent surface to the grid at each point (Tx, Ty, Tz) using Equation 1. Each point within the window (Tx_i, Ty_i, Tz_i) is presented into a spherical coordinate system to see approximately where the points are most clustered (see Watson, 1965; Woodcock, 1977).

3.2. Eigenvalues on each windowed terrain

To compute the three-dimensional eigenvalues, a windowed terrain is described as matrix B (Scheidegger, 1965; Woodcock, 1977):

$$\mathrm{B} = \begin{bmatrix} \sum {Tx_i}^2 & \sum Tx_i Ty_i & \sum Tx_i Tz_i \\ \sum Ty_i Tx_i & \sum {Ty_i}^2 & \sum Ty_i Tz_i \\ \sum Tz_i Tx_i & \sum Tz_i Ty_i & \sum {Tz_i}^2 \end{bmatrix} \div \mathrm{n} \qquad (2)$$

Each matrix element is the summation of the Cartesian representations of the tangent surface to the grid at each point (Tx_i, Ty_i, Tz_i) divided by the number of points (n) over a terrain window. Each window comprises cells (i) of three-dimensional coordinates regarded as points of slope vectors on a sphere. The eigenvalues of B are computed using the *eig* function in Matlab to represent the degree of data clustering on the unit sphere. The three eigenvalues are defined in ascending order $(\lambda_1, \lambda_2, \lambda_3)$, each representing the degree of data clustering on a Cartesian axis, where the smallest value is defined as λ_1. In the algorithm building section (see 4.1), we show that data clustering is always minimised at the vertical axis. Having the axis with the smallest eigenvalue defined, the axis of λ_2 is defined perpendicular to λ_1 and λ_3 following the right-hand rule. The eigenvalues of each Cartesian representation (Tx, Ty, Tz) are described as $(\lambda_2, \lambda_3, \lambda_1)$.

Formerly, the pattern of the spherical distribution was classified by computing logs of ratios of the three eigenvalues termed as K (see Woodcock, 1977). However, we will see in Table 1 that the vertical eigenvalue λ_1 embodies only less than 6% of the total eigenvalue in detachment terrain and less than 3% in magmatic terrain. This narrow range of vertical distribution means that the computed logs of ratios will mainly represent the pattern observed in the horizontal axis, almost neglecting the vertical component. In addition, there is no known upper limit to the computed K value, limiting the re-applicability of the formula at different settings as the range of the value is not fixed. Therefore, in our algorithm, we separate the computation into two steps. The first part focuses on the horizontal distribution of the points, and the second part focuses on the vertical distribution. The horizontal distribution of the points is observed through the eigenvalue ellipse and its horizontal eccentricity.

3.3. Eigenvalue ellipse and horizontal eccentricity

The eigenvalue ellipse is created by the horizontal eigenvalues λ_3 and λ_2, each represents the semi-major and the semi-minor axes (a and b, respectively). Illustration of the eigenvalue ellipse is presented in Figure 3.

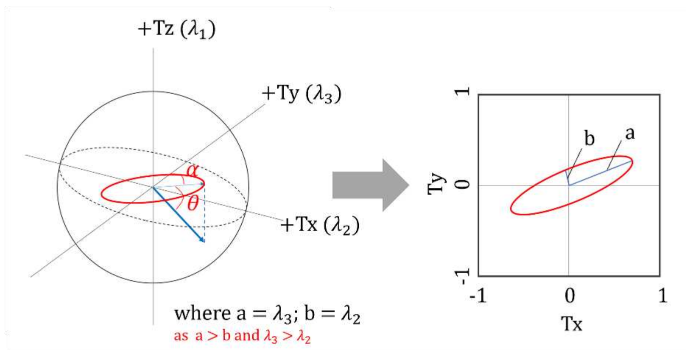

Figure 3 Illustration of the eigenvalue ellipse. The semi-major and semi-minor axes of the ellipse (a and b, respectively) are described as λ_3 and λ_2, respectively.

Mathematically, the shape of an ellipse can be characterised by a unique number termed eccentricity (e), computed based on the values of the semi-major and semi-minor axes. In particular, the eccentricity of an ellipse that is not a circle falls between $0 < e < 1$, where $e = 0$ represents a circle. Therefore, the horizontal pattern of the terrain window can be characterised using the eccentricity equation, described as:

$$\mathrm{e} = \sqrt{1 - \frac{b^2}{a^2}} = \sqrt{1 - \frac{{\lambda_2}^2}{{\lambda_3}^2}} \qquad (3)$$

The eccentricity value of a terrain window then describes the general pattern of the point in its horizontal axes. For instance, a terrain window with a high eccentricity value describes a bidirectional pattern of azimuths commonly found in magmatic terrain, as the faults are slipping parallel to each other. On the other hand, a terrain window with a low eccentricity value describes a more omnidirectional pattern of azimuth, which might indicate the presence of a detachment fault or an OCC. Having the horizontal components defined, we introduce the vertical component to have a full numerical description of the seafloor morphology. The vertical component is introduced to the computed horizontal eccentricity as a weight matrix.

3.4. Introducing slope as a weight matrix

The vertical distribution of the points can be described by the plunge (θ) parameter over the terrain window. This depth gradient can be viewed as a proxy of the fault planes over both detachment and magmatic terrain, in which normal faults indicate the presence of magmatic terrain and detachment faults indicate the latter. From the computed plunges, we generate a weight matrix that resembles the range of the eccentricity numbers computed in the previous subsection ($0 < e < 1$). The simplest way to achieve it is by computing the sine of the slope ($\sin\theta$), as the sine of $0 \leq \theta \leq 90°$ is $0 \leq \sin\theta \leq 1$. Considering the higher amount of rotation over detachment faults (Smith et al., 2008), magmatic terrain might be depicted as having a gentler slope than the detachment terrain, as the slope computes both the tilted seafloor and the well as faults.

Previously, we have learned that the eccentricity equation favours magmatic terrain with higher values than the detachment terrain. Therefore, the weight matrix must also be built to favour magmatic terrain with higher values. Considering the argument that magmatic terrain tends to be described as having gentler slopes than detachment terrain, the weight matrix W is introduced as:

$$W = 1 - \sin\theta \tag{4}$$

By introducing Equation 4 as a weight matrix to Equation 3, the 'slope-weighted eccentricity' or SWE is defined as:

$$SWE = e \times W = \sqrt{1 - \frac{{\lambda_2}^2}{{\lambda_3}^2}} \times (1 - \sin\theta) \tag{5}$$

Following the original ranges of e and W, the SWE will always fall between $0 < \text{SWE} < 1$, making it applicable to any multibeam dataset. To further identify individual OCCs, we must take into account the curvatures of the seafloor. To filter out the concave up features from the analysis, we create a mask derived from the LoG filters.

3.5. Defining curvatures with Laplacian-of-Gaussian filters

The concave up features can be masked by determining the zero-crossing of each slope from the bathymetry using the Laplacian filter (Marr and Hildreth, 1980). This space-domain filter uses curvature to discriminate long- and short-wavelength anomalies by delineating their zero-crossing points. This filter can be used to observe the general directionality and, at times, shapes and patterns of the observed signals. The two-dimensional filter can be expressed in many ways. One of them is described by Gonzalez and Woods (2002), where the filter is expressed as the linear differential operator approximating the second derivative given by:

$$\nabla^2 f = \frac{\partial^2 f}{\partial x^2} + \frac{\partial^2 f}{\partial y^2} \tag{6}$$

However, if the filter is applied directly to the original gridded bathymetry, too many edges will be detected, as a slight change of slope will be defined as a new zero-crossing. In the same study, Marr and Hildreth (1980) suggested the use of a smoothing filter before running the edge detection; hence the term Laplacian-of-Gaussian (LoG) mask (e.g., Huertas and Medioni, 1986). The Gaussian filter itself is a fixed bell-shaped response curve, essentially a space-domain low-pass filter from a specified cut-off wavelength, which is useful to mask noise and high-frequency features that might affect further operations and interpretations. According to Wells (1986), a normalised, radially symmetric, central two-dimensional Gaussian function is defined by:

$$G(x, y, \sigma) = \frac{1}{2\pi\sigma^2} e^{-(x^2+y^2)/2\sigma^2} \tag{7}$$

where σ is the standard deviation of the Gaussian filters, which represents the size of the bell-shaped curve. Physically, it represents the size of the smoothing filters, which can be determined by observing the general size of the object of interest within the study area. In our study, LoG filters are applied through the *imfilter* and *fspecial* functions of Matlab's Image Processing Toolbox.

4. Algorithm building

4.1. Calculating the eccentricity of the horizontal eigenvalues

To observe the general pattern of the two types of spreading, we select ten different windows of OCC and magmatic terrain (MTR), guided by Smith et al. (2008) interpretation. For this trial, we window the terrain with the size of 8' × 8' (~14.3 × 14.8 km), following the general size of OCCs found in the MAR (Cann et al., 1997; Cann et al., 2015; Smith et al., 2008). A more thorough sensitivity test on the window size determination will be discussed in the next step. The selected terrain windows are shown in Figure 4. From the original gridded cell size (200 m), the terrain windows are resampled into having a 15" × 15" (~446 × 462 m) cell size to optimise the computing time while maintaining quality, as well as increasing the re-applicability of the algorithm in standard computing systems. The resampling is carried out through the *grd2xyz* and *surface* functions in GMT 5.4.5 (Wessel et al., 2013).

The general pattern of the terrain can be observed from the plunge and azimuth of the slope vector. By computing these two parameters, the edges of an OCC can be depicted as having steeper slopes compared to its surroundings and dipping in an omnidirectional form (Figure 5d). On the other hand, the fault planes over magmatic terrain are also depicted as having steeper slopes compared to its surrounding, but not as steep as those found at the edges of an OCC. These slopes indicate the steep yet narrow scarps bounding the abyssal hills, which alternate in a bidirectional form (Figure 5j). The azimuth is distributed more equally in the OCC compared to a more clustered distribution in the magmatic terrain.

Each cell is then displayed in its Cartesian representations (Tx, Ty, Tz) in the form of spherical coordinate system (Figures 5e and k). From the figures, we observe that the variation in the vertical axis is not comparable to those in the horizontal axes, as the plunge values computed in the study area never surpass 30 degrees. To prove this argument, we calculate the eigenvalues of each terrain window, which results can be seen in Table 1. Based on the table, the values of λ_1 are extremely small compared to the other two eigenvalues. These values confirm the argument in 3.2. The vertical axis will always be described as λ_1, with λ_2 and λ_3 axes described consecutively following the right-hand rule.

Furthermore, we can see a directionality pattern in the ratio between λ_2 and λ_3 over both types of terrain. In the OCCs, the ratio between these two horizontal eigenvalues is not as extreme as the ratio found in the magmatic terrain. Hence, the general directionality of each window of terrain can be described in one single number by computing the eccentricity of a 'horizontal ellipse,' where λ_3 and λ_2 are defined as its semi-major and semi-minor axes, respectively (Figure 5f and l). In Table 1, we can already see that OCCs generally have a lower eccentricity value than the magmatic terrain.

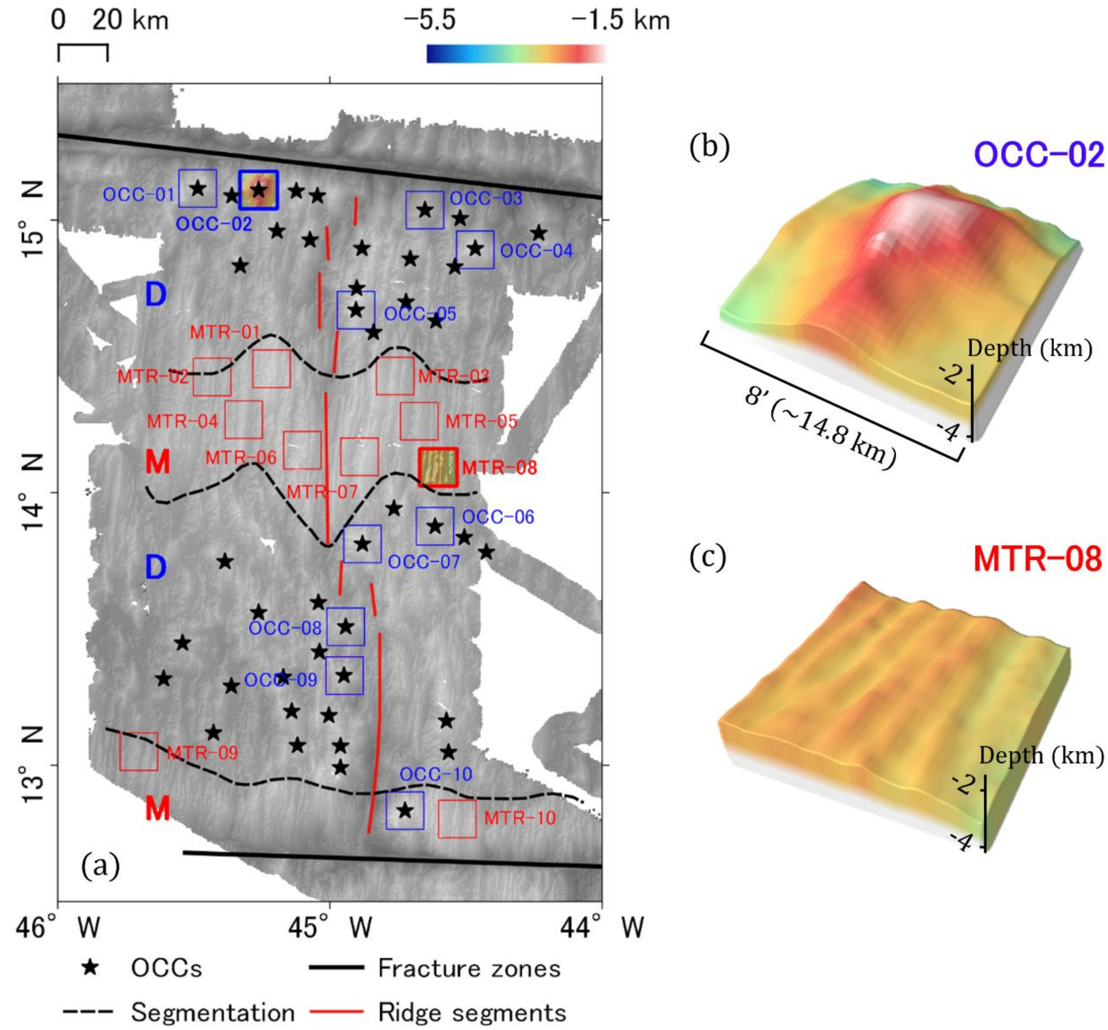

Figure 4 Distribution of windowed OCC and magmatic terrain. (a) The study area with the distribution of windowed OCC (blue squares) and magmatic terrain (red squares) used throughout the study. Inferred OCCs and segmentation (Smith et al., 2008), fracture zones, and ridge segments are identified in Figure 1. (b) Three-dimensional visualisation of an OCC terrain window. (c) Three-dimensional visualisation of a magmatic terrain window. The terrain windows shown are sampled with the size of 8’ × 8’ and 15” × 15” cell size.

Table 1 Eigen values ($\lambda_1, \lambda_2, \lambda_3$) and eccentricity ($e$) of the sampled terrain window

Oceanic core complex (OCC)					**Magmatic terrain (MTR)**				
Terrain ID	λ_1	λ_2	λ_3	e	Terrain ID	λ_1	λ_2	λ_3	e
OCC-01	0.04	0.42	0.54	0.63	MTR-01	0.01	0.26	0.73	0.94
OCC-02	0.05	0.42	0.53	0.62	MTR-02	0.01	0.17	0.82	0.98
OCC-03	0.02	0.43	0.55	0.63	MTR-03	0.02	0.23	0.75	0.95
OCC-04	0.04	0.40	0.56	0.70	MTR-04	0.01	0.17	0.81	0.98
OCC-05	0.04	0.31	0.65	0.88	MTR-05	0.02	0.18	0.81	0.98
OCC-06	0.04	0.33	0.63	0.80	MTR-06	0.03	0.18	0.80	0.97
OCC-07	0.04	0.40	0.56	0.72	MTR-07	0.01	0.17	0.80	0.98
OCC-08	0.03	0.41	0.56	0.67	MTR-08	0.01	0.20	0.79	0.97
OCC-09	0.05	0.42	0.53	0.61	MTR-09	0.01	0.27	0.72	0.93
OCC-10	0.06	0.42	0.52	0.60	MTR-10	0.01	0.26	0.73	0.94
Mean	0.04	0.40	0.56	0.69	Mean	0.01	0.21	0.78	0.96
SD	0.01	0.04	0.04	0.09	SD	0.01	0.04	0.04	0.02

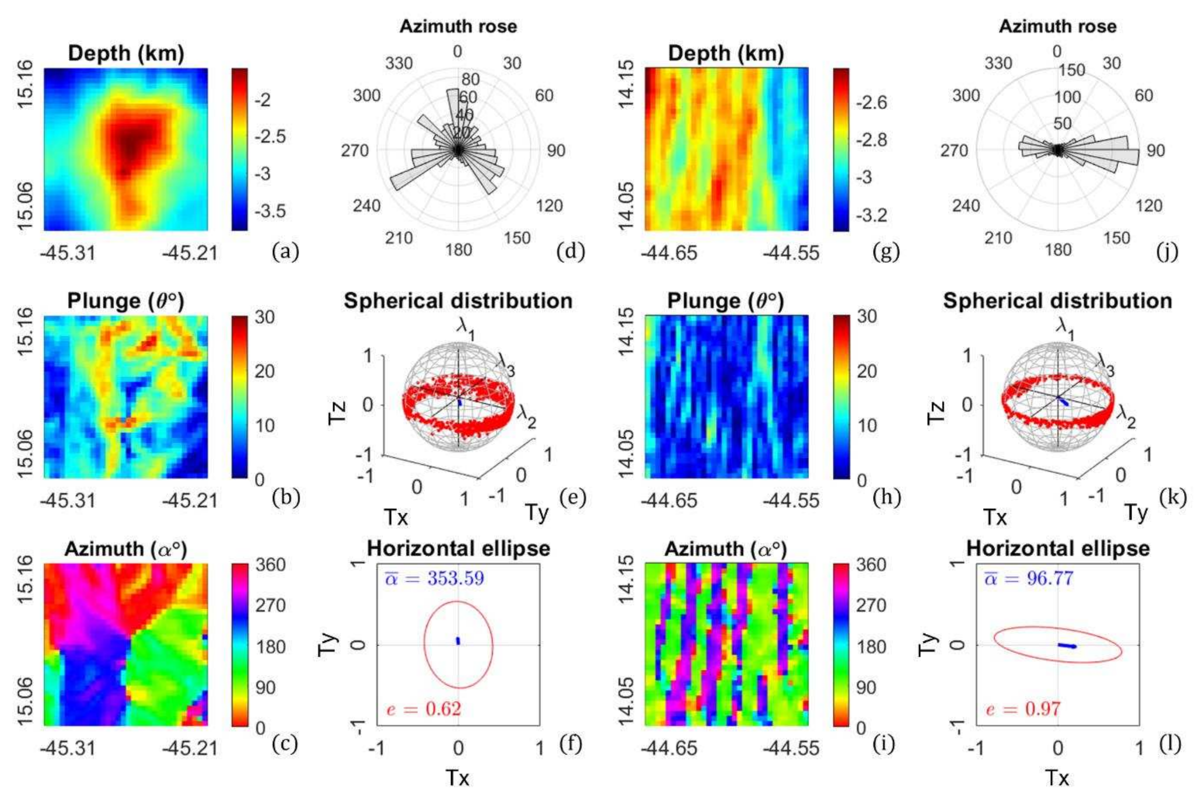

Figure 5 Directionality of OCC-02 and MTR-08 terrain windows. For OCC-02: (a) Depth in km. (b) Plunge, or θ in degrees. The edges surrounding the OCC are depicted as steeper slopes up to ~30°. (c) Azimuth, or α in degrees. The OCC is depicted as an omnidirectional feature centred at the peak of the massif. (d) Azimuth rose. (e) Spherical coordinate system. Based on the spherical distribution, variation in the vertical axis is incomparable to those in the horizontal axes. (f) Horizontal ellipse. The mean azimuth, $\bar{\alpha}$, depicts the resultant of the entire points and the eccentricity, e, describes the directional trend observed over the terrain window. For MTR-08: (g) Depth in km. (h) Plunge, or θ in degrees. The edges of the abyssal hills are depicted as gentler slopes compared to the OCC terrain window. (i) Azimuth, or α in degrees. The terrain window is depicted as consecutive bidirectional features. (j) Azimuth rose. (k) Spherical coordinate system. The variation in the vertical axis is still incomparable to those in the horizontal axes. (l) Horizontal ellipse. The eccentricity value of this terrain window is higher than in the OCC.

4.2. Determining optimum window size

The main feature that characterises the detachment mode of spreading is the presence of OCCs. The OCCs vary in shape and size, depending on which side of the ridge they are emplaced and their proximity to fracture zones or non-transform offsets. Therefore, the application of the established algorithm to the entire bathymetric grid must be preceded by determining the most effective window size that will best capture the morphology of an OCC without much interference from the surroundings.

Over the selected OCC terrain windows (Figure 6), we carried out a sensitivity test by creating windows with varying widths, ranging from 4' (~7.4 km) to 16' (~29.6 km) with a move-along interval of 2' (~3.7 km) and tested the algorithm over the terrain sampled with these varying window sizes (Figure 7). In OCC-02, for instance, the lowest value of eccentricity is computed when the window size is 16' (~29.6 km). However, the computation is largely affected by the extreme change of depth north of the OCC due to the transform fault, implying uncertainty in the computed eccentricity value. Therefore, we compute the resultant (R) of the eigenvalues $(\lambda_1, \lambda_2, \lambda_3)$ to have the overall description of the terrain directionality, defined as:

$$R = \sqrt{{\lambda_1}^2 + {\lambda_2}^2 + {\lambda_3}^2} \tag{8}$$

In Figure 7, we can observe that although the eccentricity is minimised at 16', the eigenvalue resultant is relatively large compared to the other computed eccentricity ellipses. This test is carried out on all ten windowed OCCs, and the general results can be seen in Figure 6c. The figure shows that the 8' (~14.8 km) window is the most suitable window size as it generally computes the smallest range of eccentricities. Based on these results, we opt to use 8' as the window size to run the algorithm to the entire gridded multibeam dataset.

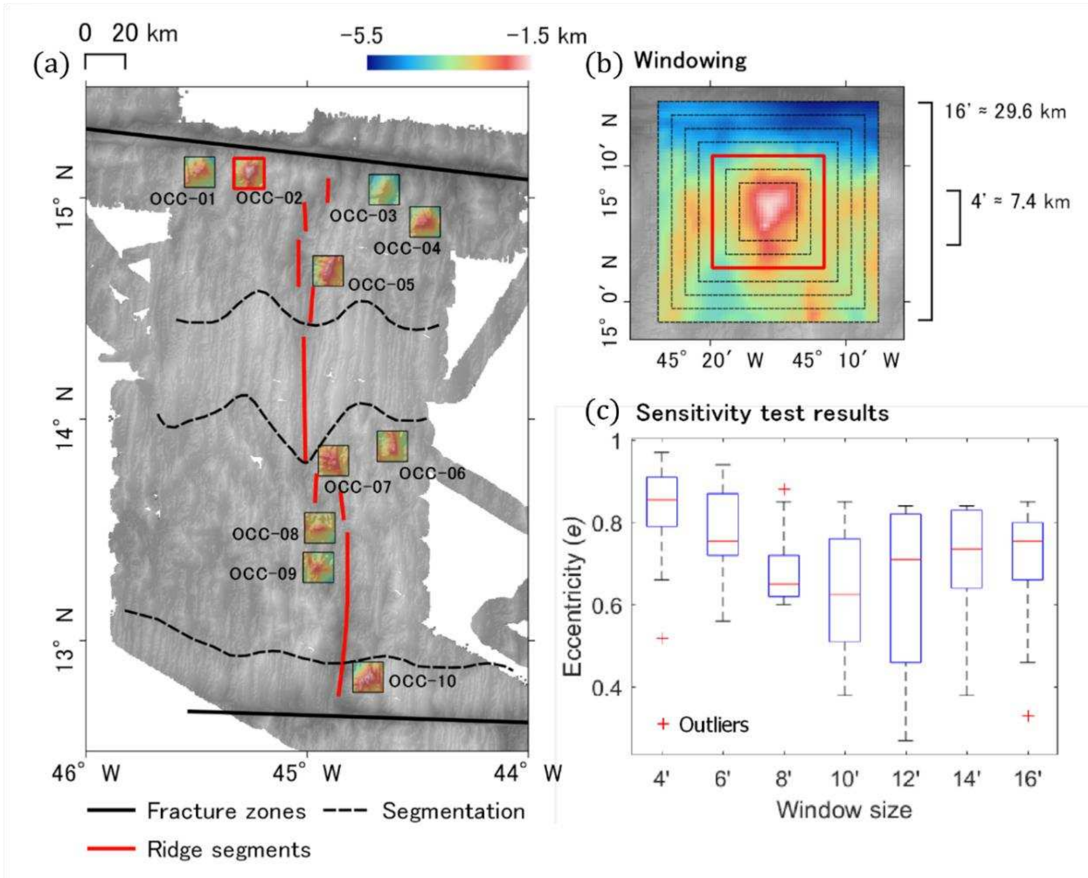

Figure 6 Sensitivity test to determine the optimum window size. (a) The ten OCCs selected for the sensitivity test. The selection is aided by the interpretation of Smith et al. (2008). (b) Illustration of OCC windowing using OCC-02. The window size varies from 4’ (~7.4 km) to 16’ (~29.6 km). Dashed square: windows with varying sizes. Red square: best-fit window. (c) Sensitivity test result, each with the sample size of ten OCCs. Each window size is presented as box and whiskers plots. The red line in each box and whiskers plot is the median eccentricity value of each window size, the ‘box’ shows the interquartile range of the eccentricity values (from Q1, or lower quartile, to Q3, or upper quartile), and the ‘whiskers’ the minimum and maximum eccentricity values Red crosses are eccentricity values indicated as outliers. The plot illustrates that the window size of 8’ (∼14.8 km) is the best fit as it delivers the smallest range of eccentricities.

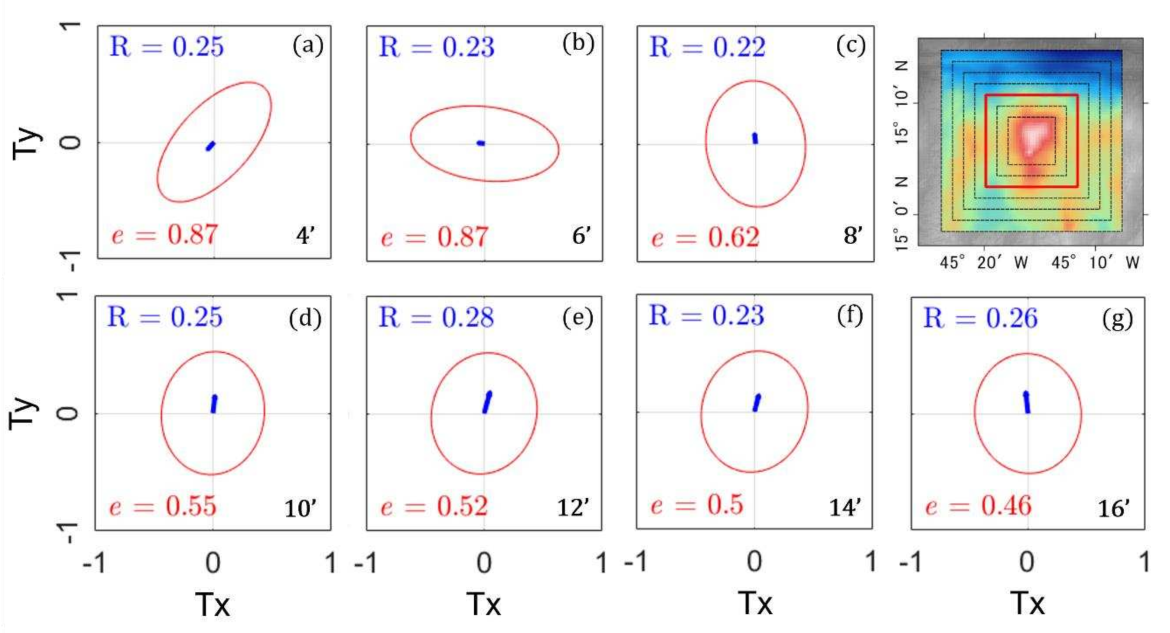

Figure 7 Windowing over the OCC-02 terrain window. Figures (a) to (g) are eigenvalue ellipses with window sizes varying from 4’ (~7.4 km) to 16’ (~29.6 km), illustrated in the index map (top-right corner). Although the 8’ (~14.8 km) window size (c) does not return the lowest eccentricity value on this OCC, it returns a relatively consistent range of eccentricity values when applied to the other OCCs as it computes the directional component of the OCC without much interference from the surrounding. For instance, the 16’ window (g) computation is largely affected by the extreme change of depth at the north, depicted in its relatively large eigenvalue resultant, *R* compared to the other windows.

4.3. Building the weight matrix

In 3.4., we presume that the magmatic terrain might be depicted as having gentler slopes compared to the detachment terrain, as the detachment terrain experienced larger rotation compared to the magmatic terrain (Smith et al., 2008). To prove this hypothesis, we compute the slopes of all the sampled OCCs and magmatic terrain windows and examine their histograms. In Figure 8, we can see that the slope observed over an OCC falls between 0° and 30°, consistent with the observation of Smith et al. (2006) and Smith et al. (2008). A gradual change is observed from one frequency bin to another, depicting the moderate change of slope forming the dome-shaped feature. The mean values of the slope histograms fall between 9.1° and 14°. On the other hand, in Figure 9, the range of the slopes observed over the magmatic terrain is generally narrower than those observed in the OCCs. In addition, we can see a larger variance in the distribution in the OCCs compared to the MTRs. The mean value of the slope falls between 5.2° and 8.1°. These values are lower than the mean slope values at the OCCs, confirming the hypothesis. The computed slopes of the OCC-02 and MTR-08 terrain windows are shown in Figure 10 to observe the spatial extent of the constructed weight matrix. The slopes surrounding the OCC are computed as steeper slopes compared to those bounding the abyssal hills in the magmatic terrain. However, the eccentricity calculation favours magmatic terrain with higher values compared to the OCC, as high eccentricity values represent a bidirectional trend of dipping slopes. Therefore, the consecutive weight matrix must be built based on the early classification obtained from the eccentricity of the horizontal eigenvalues. Lower weight must be assigned to terrain windows containing potential OCCs. From this understanding, Equation 4 is defined.

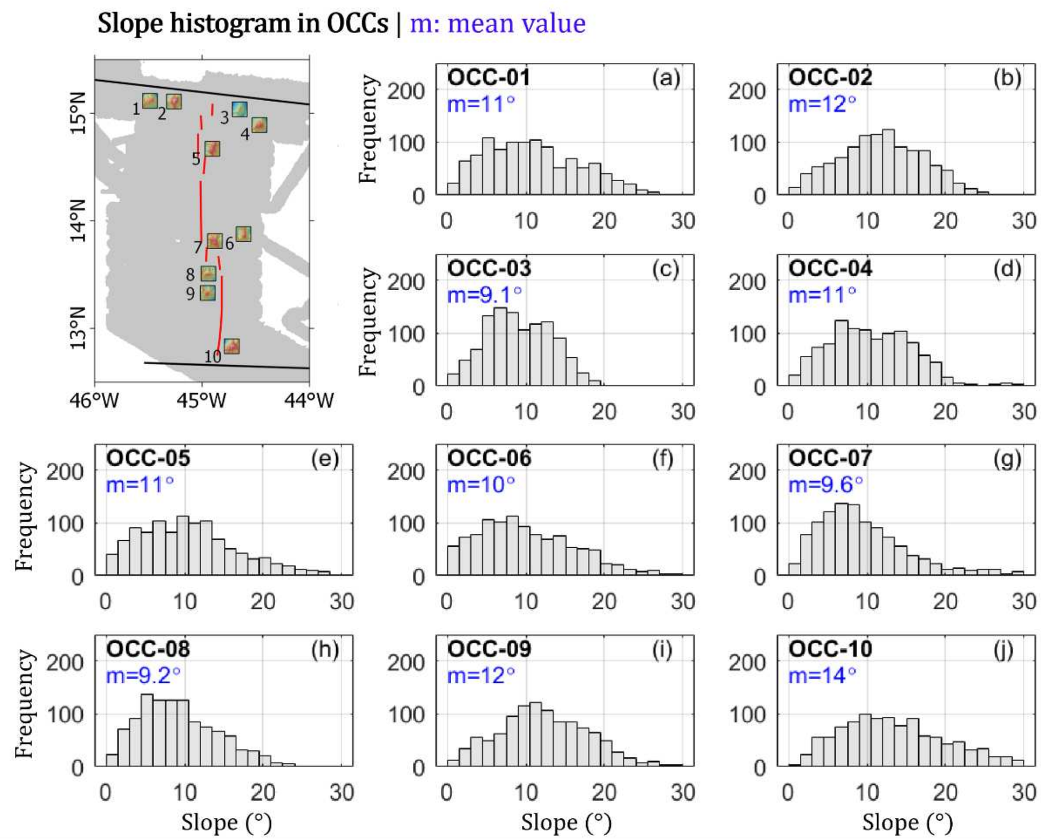

Figure 8 Slope histogram of the sampled OCCs. Histograms of the slopes observed on OCC-01 to OCC-10 are shown in (a) to (j), with locations depicted in the inset. A gradual change is observed from one frequency bin to another, depicting the moderate change of the omnidirectional slopes observed on an OCC. A bell-shaped distribution mimicking the Gaussian normal distribution is observed at OCC-02 as the size of the OCC matches quite well with the size of the window, and the shape of this particular OCC mimics the shape of a dome centred within the windowed area. A highly skewed distribution is found at OCC-07 as the breakaway zone of the OCCs is indicated by a steep-dipping slope facing away from the axis. The mean value of the slopes observed over these OCCs falls between 9.1° and 14°.

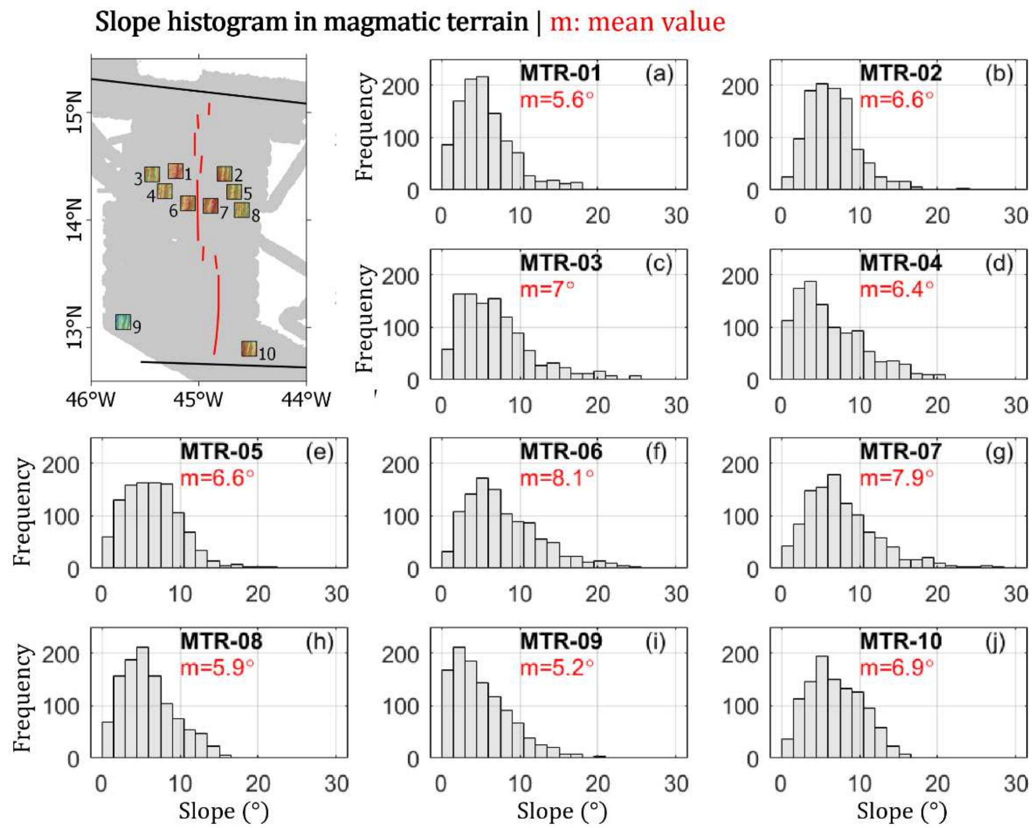

Figure 9 Slope histogram of the sampled magmatic terrain. Histograms of the slopes observed on MTR-01 to MTR-10 are shown in (a) to (j), with locations depicted in the inset. A more extreme change is observed from one frequency bin to another, specifically starting from around 5°-10°. This extreme change depicts the scarcity of steep slopes over this type of terrain. The largely skewed distribution depicts the domination of the 'background,' or the 'flat' values compared to the steep-dipping slopes. The histogram closest to a normal distribution is found in MTR-10, as the windowed terrain is still in proximity to an OCC. The mean value of the slopes observed over these windows falls between 5.2° and 8.1°, lower than the mean slope values at the OCCs.

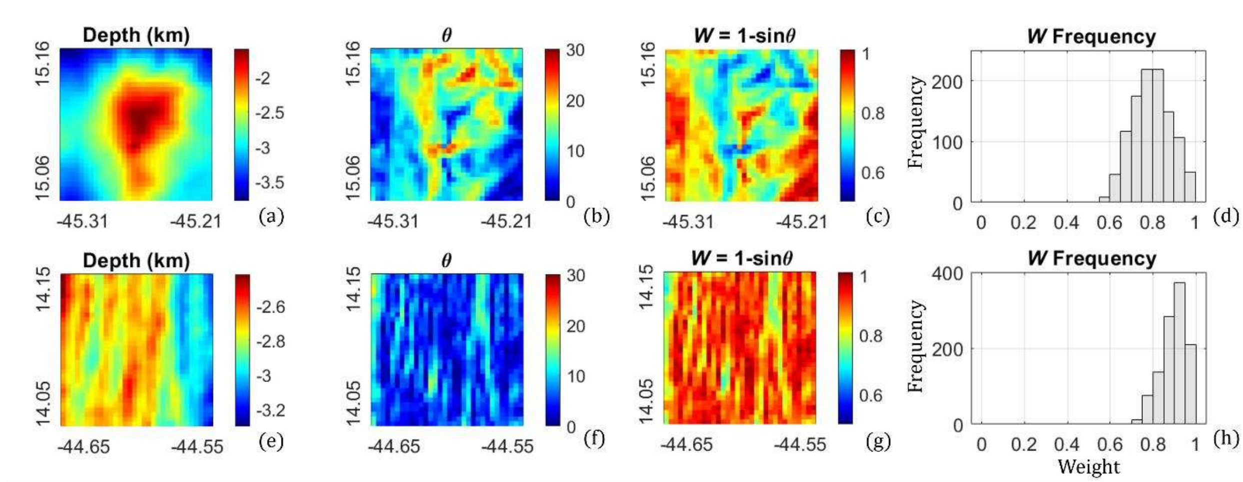

Figure 10 Computing the weight matrix over an OCC: (a) The bathymetry (depth) of OCC-02 gridded at 15” with an 8’ window size. (b) Computed slope (θ). The OCC is surrounded by an omnidirectional steep-dipping slope, depicting the rotation experienced by the seafloor through detachment faulting. (c) Computed weight matrix (W). The OCC is indicated by cells with lower W values. (d) The histogram of the W matrix over an OCC. The distribution mimics the Gaussian normal distribution curve, with a mean value of ~0.8. The normal distribution depicts the omnidirectional dipping slopes characterising the OCCs in detachment terrain. Computing the weight matrix over MTR-08: (e) The bathymetry (depth) of the sampled magmatic terrain gridded at 15” with an 8’ window size. (f) Computed slope (θ). The magmatic terrain is characterised by sparse, parallel, gentle dipping slopes scattered over the sampled area, depicting the smaller amount of rotation experienced by the magmatic seafloor. (g) Computed weight matrix (W). The magmatic terrain is indicated by cells with higher W values. (h) The histogram of the W matrix over a sampled magmatic terrain. Compared to the distribution observed at an OCC, this distribution is skewed, following the general distribution of the slopes. The highly skewed distribution ensures that areas dominated by magmatic spreading will be indicated by cells with much higher W values than those in the detachment terrain.

5. Results

5.1. Characterising the different types of spreading

The established algorithm is applied to the entire multibeam data set to assess its performance. Figure 11 shows a general result of how the eccentricity, weight matrix, and SWE calculation work. In Figure 11b, we can see how areas dominated by omnidirectional dipping slopes are quantified as having lower eccentricity numbers (e.g., areas in proximity to the bounding fracture zones). In comparison, areas dominated by bidirectional dipping slopes are quantified as having higher eccentricity numbers (e.g., the area in the middle of the ridge segment). Figure 11c shows how the weight matrix assigns lower weight to areas dominated by faults and tilted terrain. Specifically, we can observe that areas close to the bounding fracture zones are assigned lower weight, in line with the definition resulting from the eccentricity calculation. The complete SWE grid is presented in Figure 11d, in which the weight matrix is applied to the computed eccentricity. The figure shows how the SWE can classify the types of spreading by assigning cells with certain values based on the parameterisation carried out in the sampled terrain windows.

From the SWE grid shown in Figure 11d, we examine the distribution of the SWE values in the ten windowed OCC and magmatic terrain to define the boundaries of the oceanic crust formed by the different types of spreading. We display our observation in the form of box and whiskers plot shown in Figure 12. The box and whiskers plots show that the SWE values in the sampled OCCs are generally lower than those observed in the sampled magmatic terrain. The variation of SWE values is higher in the OCC samples compared to the magmatic terrain. From the distribution, we select the highest mean SWE value from the sampled OCCs as the uppermost boundary of the detachment terrain (D). The value of this boundary is 0.68, with a standard deviation of ± 0.09. The standard deviation is computed from the SWE values in the consecutive terrain window, i.e., the OCC-05. The lowest mean SWE value of the sampled magmatic terrain (M) defines the other boundary, which is 0.80, with a standard deviation of ± 0.07. As the bounding values have been defined, the remaining terrain is described as the extended terrain (E), where $0.68 < SWE < 0.80$. The extended terrain represents a buffer zone where both omnidirectional and bidirectional dipping slopes/faults exist, showing the transition from detachment to magmatic spreading or vice versa. The SWE values of this buffer zone also lie within the standard deviation of the uppermost limit of the detachment terrain and the lowermost limit of the magmatic terrain.

Having the ranges quantified, we simplify the colour bar of the SWE grid in Figure 11d into three different classes: detachment terrain (SWE ≤ 0.68), extended terrain (0.68 < SWE < 0.8), and magmatic terrain (SWE ≥ 0.8), which can be seen in Figure 13. According to the classification, 41% of the seafloor in our study area experienced detachment spreading, while 34% and 25% of the area experienced extended and magmatic spreading, respectively. The results are compared to the seismicity documented in Smith et al. (2003) and the visual interpretation of Smith et al. (2008). The detachment terrain defined by the SWE algorithm correlates well with areas previously interpreted as detachment terrain, where greater seismicity is observed and where the interpreted OCCs are in place. However, a complex alternation between the detachment and magmatic terrain is observed in the southernmost segment. We argue that our established algorithm improves the previous interpretation, in which the southernmost segment was previously defined as being dominated solely by magmatic terrain. The results also show the efficacy of the algorithm, at least when applied in typical slow-spreading ridge.

5.2. Identifying individual OCCs

After classifying the area into detachment, extended, and magmatic terrain, we take into account the curvature of the seafloor to differentiate the concave down features from the concave up features. This differentiation is important as the SWE algorithm still describes local basins with similar SWE values as those computed over the OCCs. The description occurs as the two distinct features are governed by a similar trend of directionality (Figures 14a and b). Therefore, we create a mask aided by the LoG filters to eliminate concave up features whose size and directionality mimic those found in OCCs, as well as transform faults and non-transform offsets. In this study, we apply the LoG filters through the *imfilter* and *fspecial* functions in Matlab's Image Processing Toolbox.

A rotationally symmetric LoG filter is built with a diameter equivalent to the assigned window size (8' or ~14.8 km), mimicking the general size of OCCs found in the study area. This diameter ensures that each window will only contain one OCC instead of several concave down features (e.g., domes) defined by multiple zero crossings detected by the Laplacian filters. The resulting grid is used as a mask to remove areas with concave up features (e.g., local basins) from the SWE grid. The remaining area is shown in Figure 14c, in which the local basins have been removed from the SWE grid. We can then highlight the individual OCCs by removing areas indicated as extended and magmatic terrain (Figure 14d).

According to the classification, 28% of the features within the study area are indicated as OCCs. The results correlate well with the OCCs inferred by Smith et al. (2008) and potentially indicate other OCCs that have not been previously defined (Figures 14e, f, and g). However, we can see the effect of the size of the LoG filter in the two adjacent OCCs depicted in Figure 14g. As the two OCCs are about half the size of the LoG filter and are in proximity to each other, the two distinct features are defined as one. This challenge could be dealt with by modifying the size of the LoG filter.

5.3. Discussions on varying data resolution and spreading rates

The experiment presented in this study is carried out using a multibeam data set with an original gridded resolution of 200 m. To optimise computing time, the data is resampled into having a 15” × 15” (~446 × 462 m) cell size. This choice of cell size is considerably low compared to the resolution of modern multibeam data, which could cover less than 10 m resolution. However, in Figure 15, we show that the algorithm is adequate to classify the types of terrain (detachment or magmatic) as well as identifying individual OCCs with coarser data resolution, at least up to 30” × 30” (~892 × 925 m) cell size. In addition, publicly available multibeam data, e.g., the Global Multi-Resolution Topography/GMRT (Ryan et al., 2009), has the finest, non-super sampled resolution of 122 m. This data availability strengthens our argument that the SWE method could potentially be applied to other publicly available locations other than newly obtained field data.

In the case of varying spreading rates, it is important to note that the SWE algorithm is built based on the shape, size, and directionality of the feature of interest. This study focuses solely on the features identified in slow-spreading ridges, which are the fault-bounded abyssal hills and OCCs. As the types of features might differ in varying spreading rates, a study on the quantification of the features of interest must be carried out before applying the SWE. However, as the SWE algorithm classification depends closely on the directionality of the features of interest, we argue that it would aid the identification of bidirectionally-dipping fault-bounded features that characterise magmatic spreading and a more omnidirectionally dipping amagmatic features other than OCCs. It also important to identify the sizes of the features of interest to determine the size of the moving window and LoG filter. This study uses 8’ × 8’ (~14.3 × 14.8 km) based on the general size of OCCs found in our study area, as explained in the sensitivity test is 4.2. a general study on the expected morphology and feature characterisation is advised to avoid misinterpretation at locations other than slow-spreading ridges.

6. Conclusions

We have developed a novel geomorphometric technique to automate terrain classification in slow-spreading ridges based on the shape, directionality, and curvature of a shipboard multibeam bathymetry data set. The algorithm exploits the azimuth and plunge of the seafloor to compute the dimensionless SWE values, which can be used to classify the crust dominated by either detachment or magmatic regimes based on its governing morphology. The oceanic crust in the study is thereafter classified into:

- Detachment terrain, with SWE $\leq 0.68 \pm 0.09$,
- Extended terrain, with $0.68 \pm 0.09 <$ SWE $< 0.80 \pm 0.07$, and
- Magmatic terrain, with SWE $\geq 0.80 \pm 0.07$

The detachment terrain hosts features governed by omnidirectional dipping slopes such as OCCs and local basins, while the magmatic terrain hosts features governed by bidirectional dipping faults. Between these two types, the extended terrain represents a buffer zone where both omnidirectional and bidirectional dipping slopes/faults exist, showing the transition from detachment to magmatic spreading or vice versa. This buffer zone approximately lies within the standard deviations of the uppermost limit of the detachment terrain and the lowermost limit of the magmatic terrain. The SWE values are always fixed within the range $0 < SWE < 1$, implying the re-applicability of the algorithm into various grid sets.

According to the classification, 41% of the seafloor in our study area experienced detachment spreading, with 28% of the features indicated as OCCs. This finding confirms how detachment faulting is more important in the generation of ocean crust at slow-spreading ridges than previously suspected (Smith et al., 2006). Extended and magmatic terrain governs 34% and 25% of the terrain, respectively, implying the dramatic variation of magma supply along the axis.

We suggest that the automated classification through SWE with an additional application of LoG filters can act as a novel and efficient means to provide quantitative insights into the detachment and magmatic processes that occur in a slow-spreading ridge where shipboard multibeam bathymetry data exists. This technique also widens the use of geomorphometric techniques to automate terrain classification by deriving the statistical characteristics of available multibeam bathymetry data sets. The resulting classification will serve as a substantial first step to revealing the evolution of a slow-spreading ridge through time, together with a more thorough geophysical and geochemical studies through various types of surveys, rock sampling, and laboratory analyses.

7. Acknowledgments

The authors would like to thank D. K. Smith for providing the gridded multibeam bathymetry dataset used in this study. We would also like to thank J. A. Goff, R. A. Clark, R. Parnell-Turner, A. D. Murtiyoso, B. Bramanto, N. Augustin, and two anonymous reviewers for their invaluable input to the manuscript. This work is published as part of a postgraduate research programme at the University of Leeds, funded by the Indonesian Endowment Fund for Education (LPDP).

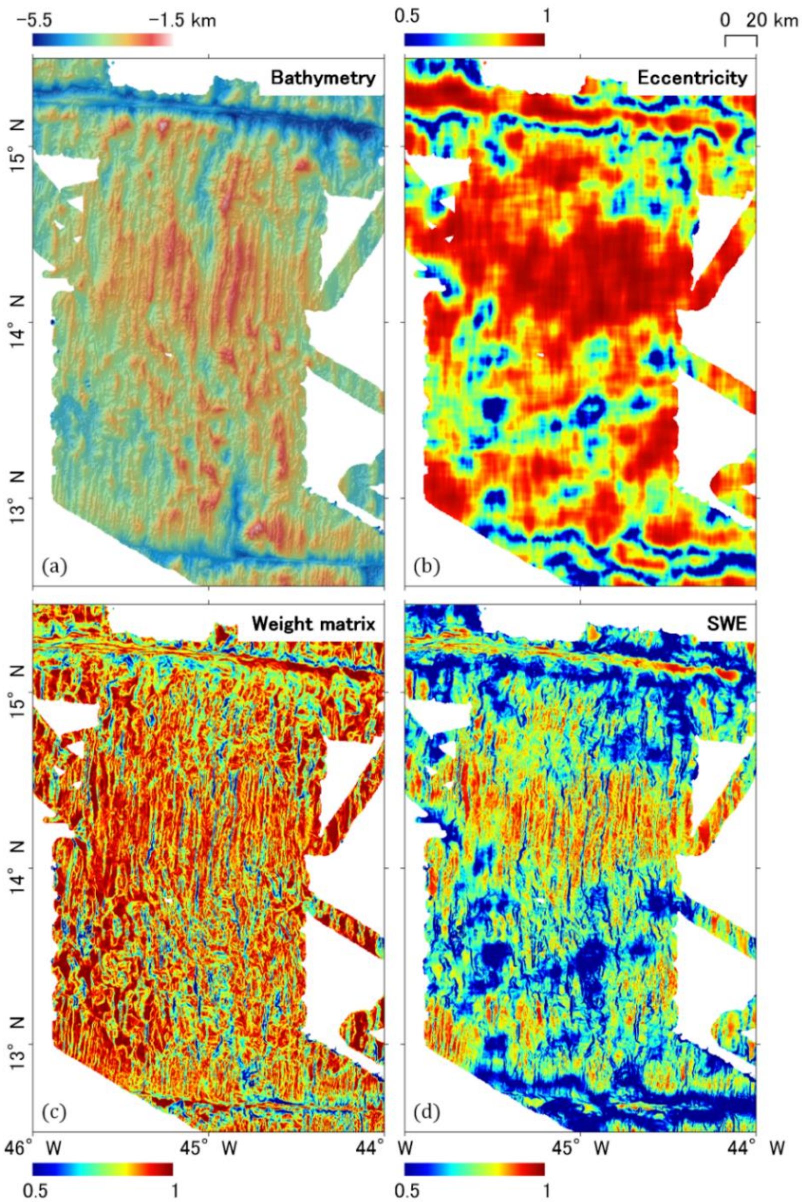

Figure 11 From bathymetry to SWE. (a) Bathymetry gridded in 15" cell size. (b) Eccentricity grid, computed from the two horizontal eigenvalues. Lower eccentricity values indicate areas composed of omnidirectional dipping slopes. (c) Weight matrix (W), computed from the slope values. Lower W values indicate cells with relatively steep slopes compared to their surroundings. (d) Slope-weighted eccentricity (SWE) grid, computed by assigning the weight matrix to the eccentricity grid. The general classification of the terrain can already be seen where lower SWE values indicate detachment terrain. The boundary between the detachment and magmatic types of spreading is examined in Figure 12.

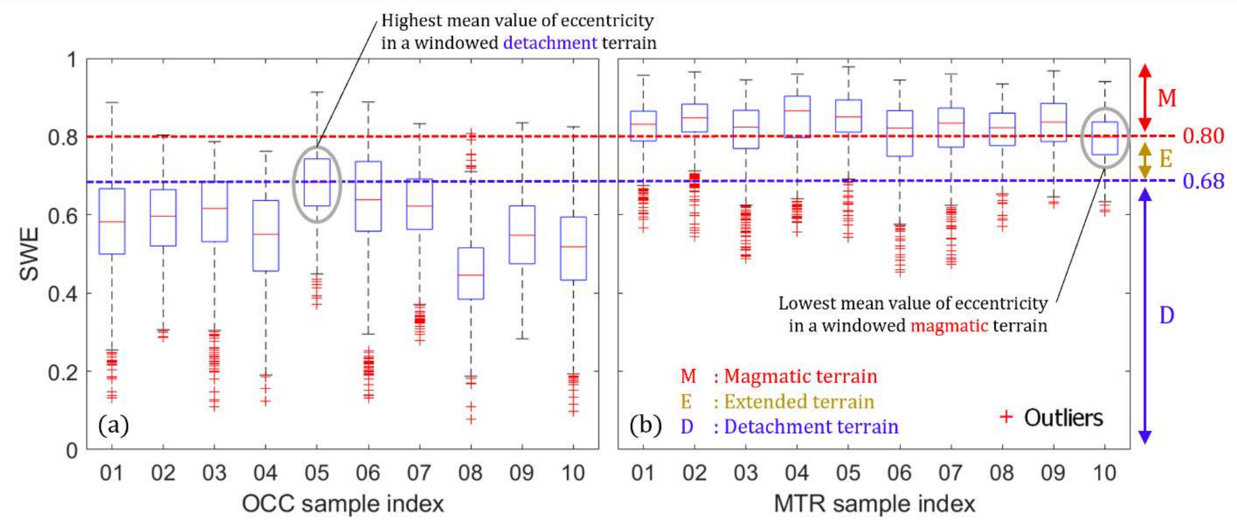

Figure 12 Terrain classification based on the SWE values computed in the sampled terrain patches. Each terrain patch is presented as box and whiskers plots. The red line in each plot is the median SWE value of each terrain patch. The box shows the interquartile range of the SWE values. The whiskers show the minimum and maximum SWE values. The red crosses are SWE values indicated as outliers. The SWE values in the sampled OCCs (a) are generally lower than those observed in the sampled magmatic terrain (b). Based on the distribution, we select the highest mean SWE value at the sampled OCCs as the uppermost boundary of the tectonic terrain (D = SWE ≤ 0.68) and the lowest mean SWE value at the lowermost boundary of the magmatic terrain (M = SWE ≥ 0.80). The standard deviation of these bounding values is computed from the SWE values in the consecutive terrain patches, i.e., the OCC with the highest mean SWE values (OCC-05) and the magmatic terrain with the lowest mean SWE values (MTR-10). The resulting standard deviation is ± 0.09 for the uppermost boundary of the detachment terrain and ± 0.07 for the magmatic terrain. SWE values between 0.68 and 0.80 are defined as extended terrain (E), in which the alteration from one type of spreading to another is commonly found.

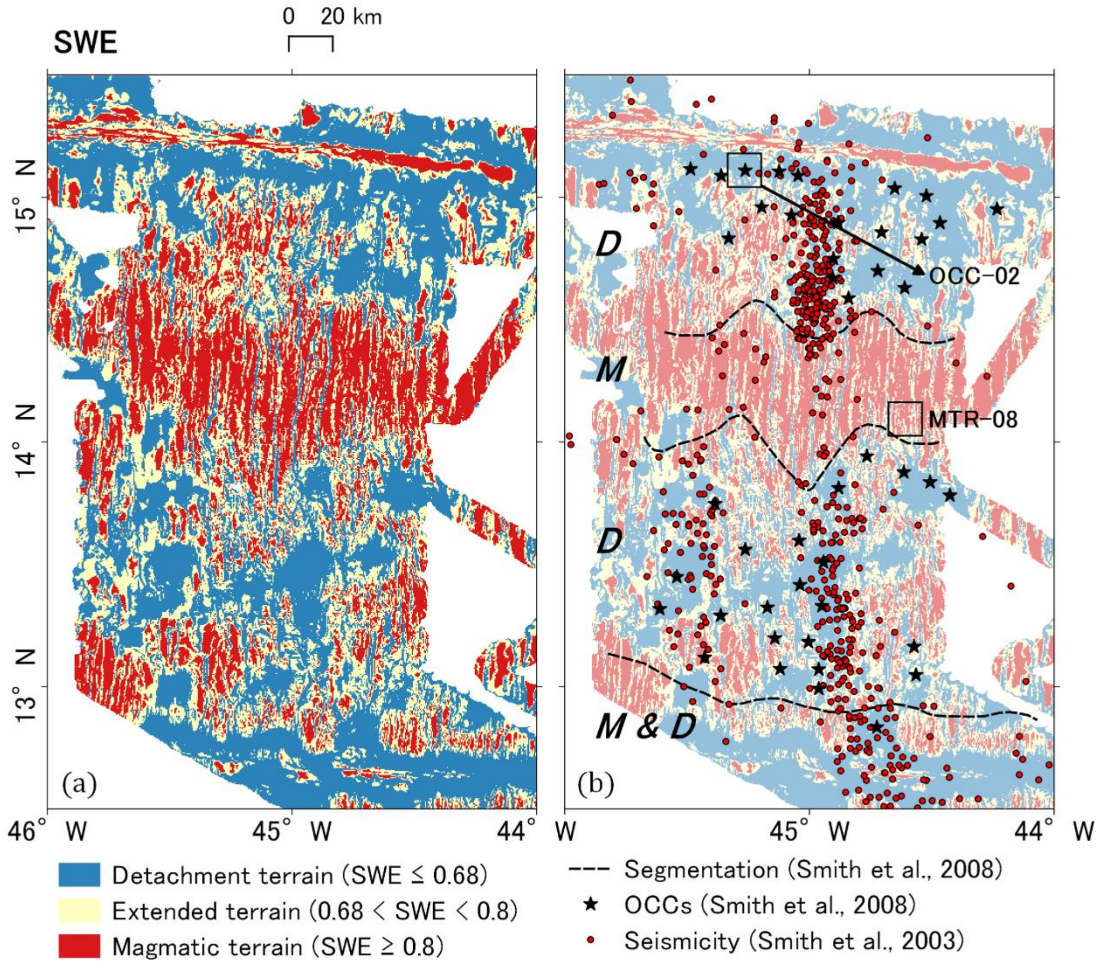

Figure 13 Terrain classification using the SWE algorithm. (a) The study area is classified based on examining the sampled OCC and magmatic terrain, shown in Figure 12. Detachment terrain is defined where SWE ≤ 0.68, extended terrain is defined where 0.68 < SWE < 0.8, and magmatic terrain is defined where SWE ≥ 0.8. (b) The SWE classification results are compared to the segmentation and OCCs interpreted by Smith et al. (2008) and seismicity documented in Smith et al. (2003). D: Detachment terrain. M: Magmatic terrain. The detachment terrain from the SWE correlates well with the areas close to the bounding fracture zones, where higher seismicity is observed, and inferred OCCs are in place. A complex alternation between the magmatic and detachment terrain is observed in the southernmost segment.

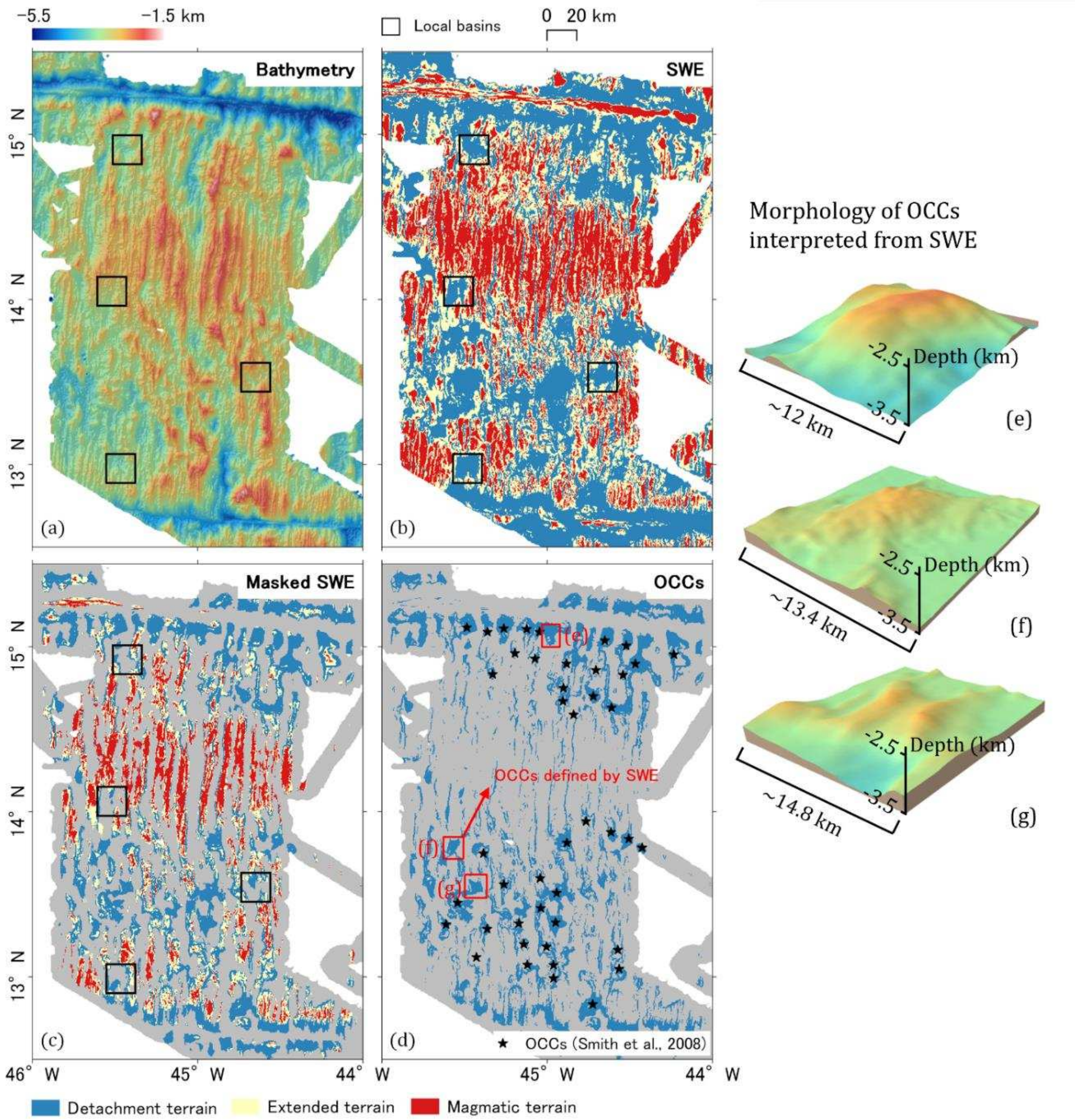

Figure 14 Identifying individual OCCs. (a) Bathymetric grid. Local basins are indicated in black squares. (b) SWE grid with local basins indicated as in the bathymetry. The SWE values of the local basins are similar to those computed over the OCCs, as a similar trend of directionality governs the two distinct features, and the curvature of the seafloor has not been taken into account. (c) Masked SWE grid. The mask is built using the LoG filter with an 8' (~14.8 km) window size, following the most suitable window size shown in Figure 6. The local basins indicated in (a) and (b) as well as transform fault areas have been removed. (d) Individual OCCs highlighted by removing areas indicated as extended and magmatic terrain. The results correlate well with the OCCs inferred by Smith et al. (2008)

and potentially indicate other undiscovered OCCs. Samples of newly indicated OCCs are highlighted with red boxes, and the bathymetry is shown in (e), (f), and (g). In (g), two OCCs are defined as one based on the size of the LoG mask. Details are discussed in the text.

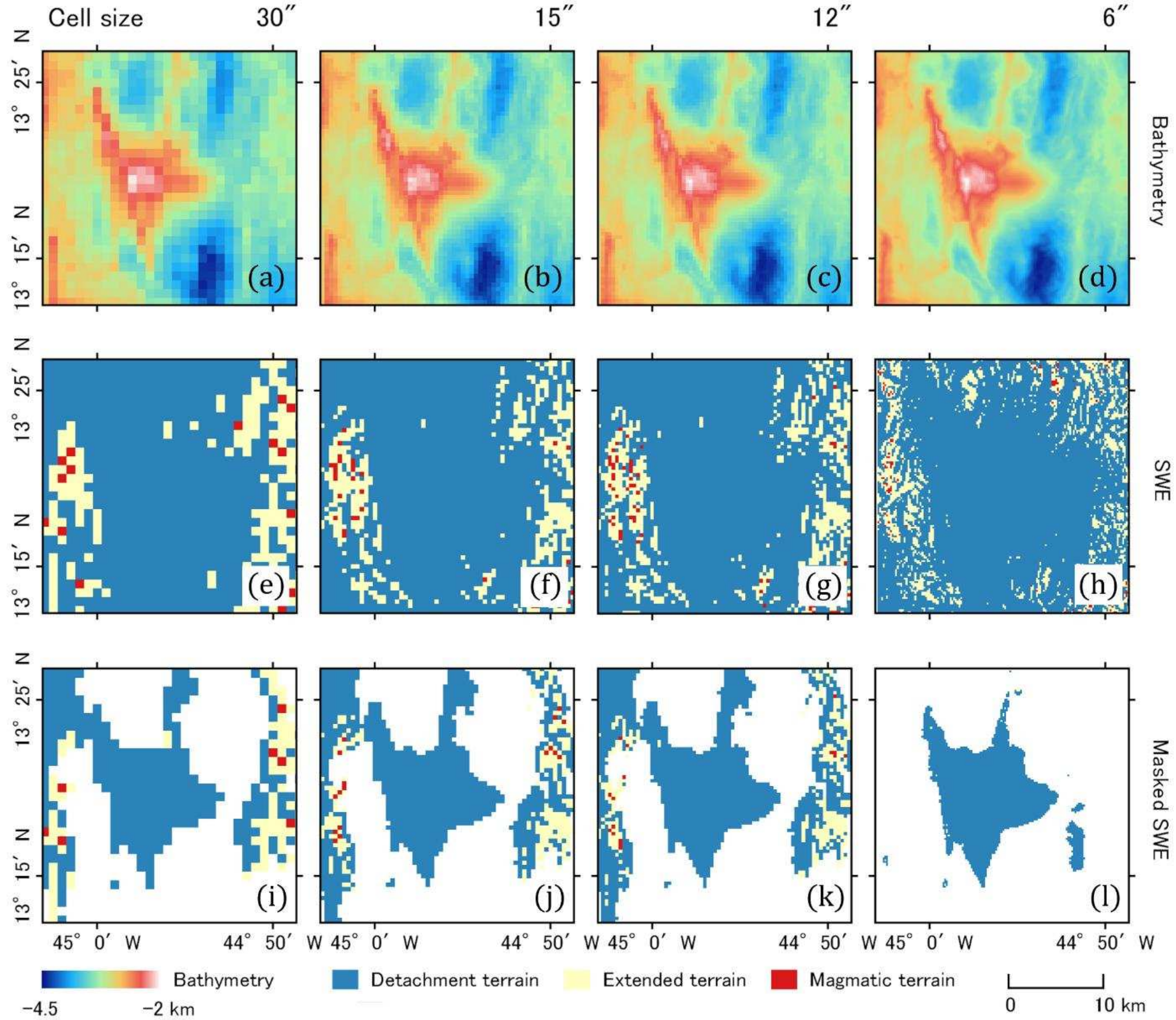

Figure 15 The effect of cell size in the SWE algorithm. The OCC-09 bathymetry (cf. Figure 4) is gridded into 30”, 15”, 12”, and 6” cell sizes, respectively, from (a) to (d). The resulting SWE interpretation of the same object is presented in (e) to (h), and the masked SWE is presented in (i) to (l). As expected, a smaller cell size (or equivalent to finer data resolution) results in a more precise interpretation of individual OCCs. However, the experiment shows that 15” (~446 × 462 m) serves as a sufficient cell size to run the SWE algorithm.

Data availability

The combined multibeam dataset originates from cruises documented in Escartín and Cannat (1999), Fujiwara et al. (2003), and Smith et al. (2006). Part of the data set can be accessed via the Global Multi-Resolution Topography MapTool, or GMRT (https://www.gmrt.org/GMRTMapTool/) after Ryan et al. (2009). The T-wave seismicity data can be accessed via NOAA's Pacific Marine Environmental Laboratory, or PMEL (http://autochart.pmel.noaa.gov:1776/autochart/GetPosit.html) after Smith et al. (2003).

Code availability

SWE_of_Bathymetry.m

Contact: gabriella.alodia@itb.ac.id / +6287737897168

Hardware requirements: The code will be most effective when used in a minimum of 8 GB RAM

Program language: The code is built in Matlab R2021a and should be compatible with any release with Image Processing Toolbox add-on

Software required: Matlab with Image Processsing Toolbox add-on

Program size: 11.2 KB (23.6 MB with data sample)

The source code and data samples are available for downloading at the link: https://github.com/gabriella-alodia/SWE_of_Bathymetry.m

References

Bergman, E.A. and Solomon, S.C., 1990. Earthquake swarms on the Mid-Atlantic Ridge: Products of magmatism or extensional tectonics? *Journal of Geophysical Research: Solid Earth*, 95(B4): 4943-4965.

Blackman, D.K., Canales, J.P. and Harding, A., 2009. Geophysical signatures of oceanic core complexes. *Geophysical Journal International, 178*(2): 593-613.

Cann, J.R., Blackman, D.K., Smith, D.K., McAllister, E., Janssen, B., Mello, S., Avgerinos, E., Pascoe, A.R. and Escartin, J., 1997. Corrugated slip surfaces formed at ridge–transform intersections on the Mid-Atlantic Ridge. *Nature*, *385*(6614), pp.329-332.

Cann, J.R., Smith, D.K., Escartin, J. and Schouten, H., 2015. Tectonic evolution of 200 km of Mid-Atlantic Ridge over 10 million years: Interplay of volcanism and faulting. *Geochemistry, Geophysics, Geosystems* *16*(7): 2303-2321.

Cannat, M., Bideau, D. and Bougault, H., 1992. Serpentinized peridotites and gabbros in the Mid-Atlantic Ridge axial valley at 15°37′N and 16°52′N. *Earth and Planetary Science Letters, 109*(1): 87-106.

Cannat, M., Lagabrielle, Y., Bougault, H., Casey, J., de Coutures, N., Dmitriev, L. and Fouquet, Y., 1997. Ultramafic and gabbroic exposures at the Mid-Atlantic Ridge: geological mapping in the 15°N region. *Tectonophysics, 279*(1): 193-213.

Chakraborty, B., Schenke, H., Kodagali, V. and Hagen, R., 2001. Analysis of multibeam-Hydrosweep echo peaks for seabed characterisation. *Geo-Marine Letters*, *20*(3), pp.174-181.

Dannowski, A., Grevemeyer, I., Ranero, C.R., Ceuleneer, G., Maia, M., Morgan, J.P. and Gente, P., 2010. Seismic structure of an oceanic core complex at the Mid-Atlantic Ridge, 22°19′N. *Journal of Geophysical Research: Solid Earth, 115*(B7).

Escartín, J. and Cannat, M., 1999. Ultramafic exposures and the gravity signature of the lithosphere near the Fifteen-Twenty Fracture Zone (Mid-Atlantic Ridge, 14°–16.5°N). *Earth and Planetary Science Letters, 171*(3): 411-424.

Escartín, J., Smith, D.K., Cann, J., Schouten, H., Langmuir, C.H. and Escrig, S., 2008. Central role of detachment faults in accretion of slow-spreading oceanic lithosphere. *Nature, 455*: 790.

Escartín, J., Smith, D.K. and Cannat, M., 2003. Parallel bands of seismicity at the Mid-Atlantic Ridge, 12–14°N. *Geophysical Research Letters, 30*(12).

Fox, C.G., Matsumoto, H. and Lau, T.-K.A., 2001. Monitoring Pacific Ocean seismicity from an autonomous hydrophone array. *Journal of Geophysical Research: Solid Earth, 106*(B3): 4183-4206.

Fujiwara, T., Lin, J., Matsumoto, T., Kelemen, P.B., Tucholke, B.E. and Casey, J.F., 2003. Crustal Evolution of the Mid-Atlantic Ridge near the Fifteen-Twenty Fracture Zone in the last 5 Ma. *Geochemistry, Geophysics, Geosystems, 4*(3).

Gafeira, J., Long, D. and Diaz-Doce, D., 2012. Semi-automated characterisation of seabed pockmarks in the central North Sea. *Near Surface Geophysics*, *10*(4), pp.301-312.

Goff, J.A. and Jordan, T.H., 1988. Stochastic Modeling of Seafloor Morphology: Inversion of Sea Beam Data for Second-Order Statistics. *Journal of Geophysical Research: Solid Earth, 93*(B11): 13589-13608.

Goff, J.A., Tucholke, B.E., Lin, J., Jaroslow, G.E. and Kleinrock, M.C., 1995. Quantitative analysis of abyssal hills in the Atlantic Ocean: A correlation between inferred crustal thickness and extensional faulting. *Journal of Geophysical Research: Solid Earth, 100*(B11): 22509-22522.

Gonzalez, R.C. and Woods, R.E., 2002. Digital image processing. Prentice hall Upper Saddle River, NJ.

Green, A. and Uken, R., 2008. Submarine landsliding and canyon evolution on the northern KwaZulu-Natal continental shelf, South Africa, SW Indian Ocean. *Marine Geology, 254*(3): 152-170.

Harrison, R., Bellec, V., Mann, D. and Wang, W., 2011, September. A new approach to the automated mapping of pockmarks in multi-beam bathymetry. In *2011 18th IEEE International Conference on Image Processing* (pp. 2777-2780). IEEE.

Huertas, A. and Medioni, G., 1986. Detection of intensity changes with subpixel accuracy using Laplacian-Gaussian masks. *IEEE Transactions on Pattern Analysis and Machine Intelligence*, (5), pp.651-664.

Ismail, K., Huvenne, V.A.I. and Masson, D.G., 2015. Objective automated classification technique for marine landscape mapping in submarine canyons. *Marine Geology, 362*: 17-32.

Kong, L.S.L., Solomon, S.C. and Purdy, G.M., 1992. Microearthquake Characteristics of a Mid-Ocean Ridge along-axis high. *Journal of Geophysical Research: Solid Earth, 97*(B2): 1659-1685.

Lagabrielle, Y., Bideau, D., Cannat, M., Karson, J.A. and MéVel, C., 1998. Ultramafic-Mafic Plutonic Rock Suites Exposed Along the Mid-Atlantic Ridge (10 N-30 N) Symmetrical-Asymmetrical Distribution and Implications for Seafloor Spreading Processes. *GEOPHYSICAL MONOGRAPH-AMERICAN GEOPHYSICAL UNION, 106*: 153-176.

Lecours, V., Dolan, M.F., Micallef, A. and Lucieer, V.L., 2016. A review of marine geomorphometry, the quantitative study of the seafloor. *Hydrology and Earth System Sciences*, *20*(8), pp.3207-3244.

Macdonald, K.C., 1982. Mid-Ocean Ridges: Fine Scale Tectonic, Volcanic and Hydrothermal Processes Within the Plate Boundary Zone. *Annual Review of Earth and Planetary Sciences, 10*(1): 155-190.

MacLeod, C.J., Searle, R.C., Murton, B.J., Casey, J.F., Mallows, C., Unsworth, S.C., Achenbach, K.L. and Harris, M., 2009. Life cycle of oceanic core complexes. *Earth and Planetary Science Letters, 287*(3): 333-344.

MacLeod, C.J., Smith, D.K., Escartín, J., Banerji, D., Banks, G.J., Gleeson, M., Irving, D.H.B., Lilly, R.M., McCaig, A.M., Niu, Y. and Allerton, S., 2002. Direct geological evidence for oceanic detachment faulting: The Mid-Atlantic Ridge, 15°45′N. *Geology, 30*(10): 879-882.

Marr, D. and Hildreth, E., 1980. Theory of edge detection. *Proceedings of the Royal Society of London. Series B. Biological Sciences*, *207*(1167), pp.187-217.

McCaig, A.M. and Harris, M., 2012. Hydrothermal circulation and the dike-gabbro transition in the detachment mode of slow seafloor spreading. *Geology, 40*(4): 367-370.

Micallef, A., Le Bas, T.P., Huvenne, V.A.I., Blondel, P., Hühnerbach, V. and Deidun, A., 2012. A multi-method approach for benthic habitat mapping of shallow coastal areas with high-resolution multibeam data. *Continental Shelf Research, 39-40*: 14-26.

Mutter, J.C. and Karson, J.A., 1992. Structural Processes at Slow-Spreading Ridges. Science, 257(5070): 627.

Passaro, S., Ferranti, L. and de Alteriis, G., 2011. The use of high-resolution elevation histograms for mapping submerged terraces: Tests from the Eastern Tyrrhenian Sea and the Eastern Atlantic Ocean. *Quaternary International, 232*(1): 238-249.

Pockalny, R.A., Smith, A. and Gente, P., 1995. Spatial and temporal variability of crustal magnetization of a slowly spreading ridge: Mid-Atlantic Ridge (20°–24° N). *Marine Geophysical Researches, 17*(3): 301-320.

Rona, P.A., Widenfalk, L. and Boström, K., 1987. Serpentinized ultramafics and hydrothermal activity at the Mid-Atlantic Ridge crest near 15°N. *Journal of Geophysical Research: Solid Earth, 92*(B2): 1417-1427.

Ryan, W.B., Carbotte, S.M., Coplan, J.O., O'Hara, S., Melkonian, A., Arko, R., Weissel, R.A., Ferrini, V., Goodwillie, A., Nitsche, F. and Bonczkowski, J., 2009. Global multi-resolution topography synthesis. *Geochemistry, Geophysics, Geosystems*, *10*(3).

Scheidegger, A.E., 1965. On the statistics of the orientation of bedding planes, grain axes, and similar sedimentological data. *US Geological Survey Professional Paper, 525*: 164-167.

Schroeder, T., Cheadle, M.J., Dick, H.J.B., Faul, U., Casey, J.F. and Kelemen, P.B., 2007. Nonvolcanic seafloor spreading and corner-flow rotation accommodated by extensional faulting at 15°N on the Mid-Atlantic Ridge: A structural synthesis of ODP Leg 209. *Geochemistry, Geophysics, Geosystems, 8*(6).

Sinton, J.M. and Detrick, R.S., 1992. Mid-ocean ridge magma chambers. *Journal of Geophysical Research: Solid Earth, 97*(B1): 197-216.

Smith, D., 2013. Mantle spread across the sea floor. *Nature Geoscience, 6*(4): 247-248.

Smith, D.K., Cann, J.R. and Escartín, J., 2006. Widespread active detachment faulting and core complex formation near 13° N on the Mid-Atlantic Ridge. *Nature, 442*(7101): 440-443.

Smith, D.K., Escartin, J., Cannat, M., Tolstoy, M., Fox, C.G., Bohnenstiehl, D.R. and Bazin, S., 2003. Spatial and temporal distribution of seismicity along the northern Mid-Atlantic Ridge (15°–35°N). *Journal of Geophysical Research: Solid Earth, 108*(B3).

Smith, D.K., Escartín, J., Schouten, H. and Cann, J.R., 2008. Fault rotation and core complex formation: Significant processes in seafloor formation at slow-spreading mid-ocean ridges (Mid-Atlantic Ridge, 13°–15°N). *Geochemistry, Geophysics, Geosystems, 9*(3).

Smith, D.K. and Shaw, P.R., 1989. Using topographic slope distributions to infer seafloor patterns. *IEEE Journal of Oceanic Engineering, 14*(4): 338-347.

Smith, D.K., Tolstoy, M., Fox, C.G., Bohnenstiehl, D.R., Matsumoto, H. and J. Fowler, M., 2002. Hydroacoustic monitoring of seismicity at the slow-spreading Mid-Atlantic Ridge. *Geophysical Research Letters, 29*(11): 13-1-13-4.

Tivey, M.A. and Dyment, J., 2010. The magnetic signature of hydrothermal systems in slow spreading environments. *Diversity of Hydrothermal Systems on Slow Spreading Ocean Ridges, Geophysical Mohograph Series, 188*, pp.43-65.

Tucholke, B.E., Behn, M.D., Buck, W.R. and Lin, J., 2008. Role of melt supply in oceanic detachment faulting and formation of megamullions. *Geology, 36*(6): 455-458.

Tucholke, B.E., Lin, J. and Kleinrock, M.C., 1998. Megamullions and mullion structure defining oceanic metamorphic core complexes on the Mid-Atlantic Ridge. *Journal of Geophysical Research: Solid Earth, 103*(B5): 9857-9866.

Watson, G.S., 1965. Equatorial Distributions on a Sphere. *Biometrika, 52*(1/2): 193-201.

Wells, W.M., 1986. Efficient synthesis of Gaussian filters by cascaded uniform filters. *IEEE Transactions on Pattern Analysis and Machine Intelligence*, (2), pp.234-239.

Wessel, P., Smith, W.H.F., Scharroo, R., Luis, J.F. and Wobbe, F., 2013. GMT 5: A major new release of the Generic Mapping Tools. *Eos, Transactions of the American Geophysical Union*, *94*(45), pp.409-410.

Wilson, M.F.J., O'Connell, B., Brown, C., Guinan, J.C. and Grehan, A.J., 2007. Multiscale Terrain Analysis of Multibeam Bathymetry Data for Habitat Mapping on the Continental Slope. *Marine Geodesy, 30*(1-2): 3-35.

Wolfe, C.J., Purdy, G.M., Toomey, D.R. and Solomon, S.C., 1995. Microearthquake characteristics and crustal velocity structure at 29°N on the Mid-Atlantic Ridge: The architecture of a slow spreading segment. *Journal of Geophysical Research: Solid Earth, 100*(B12): 24449-24472.

Woodcock, N.H., 1977. Specification of fabric shapes using an eigenvalue method. *GSA Bulletin, 88*(9): 1231-1236.

List of Figures

slopes compared to the OCC terrain window. (i) Azimuth, or α in degrees. The terrain window is depicted as consecutive bidirectional features. (j) Azimuth rose. (k) Spherical coordinate system. The variation in the vertical axis is still incomparable to those in the horizontal axes. (l) Horizontal ellipse. The eccentricity value of this terrain window is higher than in the OCC.

6. Figure 6: Sensitivity test to determine the optimum window size. (a) The ten OCCs selected for the sensitivity test. The selection is aided by the interpretation of Smith et al. (2008). (b) Illustration of OCC windowing using OCC-02. The window size varies from 4’ (~7.4 km) to 16’ (~29.6 km). Dashed square: windows with varying sizes. Red square: best-fit window. (c) Sensitivity test result, each with the sample size of ten OCCs. Each window size is presented as box and whiskers plots. The red line in each box and whiskers plot is the median eccentricity value of each window size, the ‘box’ shows the interquartile range of the eccentricity values (from Q1, or lower quartile, to Q3, or upper quartile), and the ‘whiskers’ the minimum and maximum eccentricity values. Red crosses are eccentricity values indicated as outliers. The plot illustrates that the window size of 8’ (∼14.8 km) is the best fit as it delivers the smallest range of eccentricities.
7. Figure 7: Windowing over the OCC-02 terrain window. Figures (a) to (g) are eigenvalue ellipses with window sizes varying from 4’ (~7.4 km) to 16’ (~29.6 km), illustrated in the index map (top-right corner). Although the 8’ (~14.8 km) window size (c) does not return the lowest eccentricity value on this OCC, it returns a relatively consistent range of eccentricity values when applied to the other OCCs as it computes the directional component of the OCC without much interference from the surrounding. For instance, the 16’ window (g) computation is largely affected by the extreme change of depth at the north, depicted in its relatively large eigenvalue resultant, R compared to the other windows.
8. Figure 8: Slope histogram of the sampled OCCs. Histograms of the slopes observed on OCC-01 to OCC-10 are shown in (a) to (j), with locations depicted in the inset. A gradual change is observed from one frequency bin to another, depicting the moderate change of the omnidirectional slopes observed on an OCC. A bell-shaped distribution mimicking the Gaussian normal distribution is observed at OCC-02 as the size of the OCC matches quite well with the size of the window, and the shape of this particular OCC mimics the shape of a dome centred within the windowed area. A highly skewed distribution is found at OCC-07 as the breakaway zone of

the OCCs is indicated by a steep-dipping slope facing away from the axis. The mean value of the slopes observed over these OCCs falls between 9.1° and 14°.

9. Figure 9: Slope histogram of the sampled magmatic terrain. Histograms of the slopes observed on MTR-01 to MTR-10 are shown in (a) to (j), with locations depicted in the inset. A more extreme change is observed from one frequency bin to another, specifically starting from around 5°-10°. This extreme change depicts the scarcity of steep slopes over this type of terrain. The largely skewed distribution depicts the domination of the 'background,' or the 'flat' values compared to the steep-dipping slopes. The histogram closest to a normal distribution is found in MTR-10, as the windowed terrain is still in proximity to an OCC. The mean value of the slopes observed over these windows falls between 5.2° and 8.1°, lower than the mean slope values at the OCCs.
10. Figure 10: Computing the weight matrix over an OCC: (a) The bathymetry (depth) of OCC-02 gridded at 15" with an 8' window size. (b) Computed slope (θ). The OCC is surrounded by an omnidirectional steep-dipping slope, depicting the rotation experienced by the seafloor through detachment faulting. (c) Computed weight matrix (W). The OCC is indicated by cells with lower W values. (d) The histogram of the W matrix over an OCC. The distribution mimics the Gaussian normal distribution curve, with a mean value of ~0.8. The normal distribution depicts the omnidirectional dipping slopes characterising the OCCs in detachment terrain. Computing the weight matrix over MTR-08: (e) The bathymetry (depth) of the sampled magmatic terrain gridded at 15" with an 8' window size. (f) Computed slope (θ). The magmatic terrain is characterised by sparse, parallel, gentle dipping slopes scattered over the sampled area, depicting the smaller amount of rotation experienced by the magmatic seafloor. (g) Computed weight matrix (W). The magmatic terrain is indicated by cells with higher W values. (h) The histogram of the W matrix over a sampled magmatic terrain. Compared to the distribution observed at an OCC, this distribution is skewed, following the general distribution of the slopes. The highly skewed distribution ensures that areas dominated by magmatic spreading will be indicated by cells with much higher W values than those in the detachment terrain.
11. Figure 11: From bathymetry to SWE. (a) Bathymetry gridded in 15" cell size. (b) Eccentricity grid, computed from the two horizontal eigenvalues. Lower eccentricity values indicate areas composed of omnidirectional dipping slopes. (c) Weight matrix (W), computed from the slope values. Lower W values indicate cells with relatively steep slopes compared to their surroundings. (d) Slope-weighted eccentricity (SWE) grid, computed

by assigning the weight matrix to the eccentricity grid. The general classification of the terrain can already be seen where lower SWE values indicate detachment terrain. The boundary between the detachment and magmatic types of spreading is examined in Figure 12.

12. Figure 12: Terrain classification based on the SWE values computed in the sampled terrain patches. Each terrain patch is presented as box and whiskers plots. The red line in each plot is the median SWE value of each terrain patch. The box shows the interquartile range of the SWE values. The whiskers show the minimum and maximum SWE values. The red crosses are SWE values indicated as outliers. The SWE values in the sampled OCCs (a) are generally lower than those observed in the sampled magmatic terrain (b). Based on the distribution, we select the highest mean SWE value at the sampled OCCs as the uppermost boundary of the tectonic terrain (D = SWE $\leq$ 0.68) and the lowest mean SWE value at the lowermost boundary of the magmatic terrain (M = SWE $\geq$ 0.80). The standard deviation of these bounding values is computed from the SWE values in the consecutive terrain patches, i.e., the OCC with the highest mean SWE values (OCC-05) and the magmatic terrain with the lowest mean SWE values (MTR-10). The resulting standard deviation is $\pm$ 0.09 for the uppermost boundary of the detachment terrain and $\pm$ 0.07 for the magmatic terrain. SWE values between 0.68 and 0.80 are defined as extended terrain (E), in which the alteration from one type of spreading to another is commonly found.
13. Figure 13: Terrain classification using the SWE algorithm. (a) The study area is classified based on examining the sampled OCC and magmatic terrain, shown in Figure 12. Detachment terrain is defined where SWE $\leq$ 0.68, extended terrain is defined where 0.68 $<$ SWE $<$ 0.8, and magmatic terrain is defined where SWE $\geq$ 0.8. (b) The SWE classification results are compared to the segmentation and OCCs interpreted by Smith et al. (2008) and seismicity documented in Smith et al. (2003). D: Detachment terrain. M: Magmatic terrain. The detachment terrain from the SWE correlates well with the areas close to the bounding fracture zones, where higher seismicity is observed, and inferred OCCs are in place. A complex alternation between the magmatic and detachment terrain is observed in the southernmost segment.
14. Figure 14: Identifying individual OCCs. (a) Bathymetric grid. Local basins are indicated in black squares. (b) SWE grid with local basins indicated as in the bathymetry. The SWE values of the local basins are similar to those computed over the OCCs, as a similar trend of directionality governs the two distinct features, and the

curvature of the seafloor has not been taken into account. (c) Masked SWE grid. The mask is built using the LoG filter with an 8’ (~14.8 km) window size, following the most suitable window size shown in Figure 6. The local basins indicated in (a) and (b) as well as transform fault areas have been removed. (d) Individual OCCs highlighted by removing areas indicated as extended and magmatic terrain. The results correlate well with the OCCs inferred by Smith et al. (2008) and potentially indicate other undiscovered OCCs. Samples of newly indicated OCCs are highlighted with red boxes, and the bathymetry is shown in (e), (f), and (g). In (g), two OCCs are defined as one based on the size of the LoG mask. Details are discussed in the text.

15. Figure 15: The effect of cell size in the SWE algorithm. The OCC-09 bathymetry (cf. Figure 4) is gridded into 30”, 15”, 12”, and 6” cell sizes, respectively, from (a) to (d). The resulting SWE interpretation of the same object is presented in (e) to (h), and the masked SWE is presented in (i) to (l). As expected, a smaller cell size (or equivalent to finer data resolution) results in a more precise interpretation of individual OCCs. However, the experiment shows that 15” (~446 × 462 m) serves as a sufficient cell size to run the SWE algorithm.

List of Tables